A multiplex platform to identify mechanisms and modulators of proteotoxicity in neurodegeneration

Samuel J. Resnick[1,2,3], Seema Qamar[4], Jenny Sheng[1,3], Lei Haley Huang[1], Jonathon Nixon-Abell[4], Schuyler Melore[1], Chyi Wei Chung[5], Xuecong Li[6], Jingshu Wang[7], Nancy Zhang[8], Neil A. Shneider[9,10], Clemens F. Kaminski[5], Francesco Simone Ruggeri[6,11], Gabriele S. Kaminski Schierle[5], Peter St George-Hyslop[4,12,13], Alejandro Chavez[1,9,*]

[1] Department of Pathology and Cell Biology, Columbia University Irving Medical Center, New York, NY, 10032, USA

[2] Medical Scientist Training Program, Columbia University Irving Medical Center, New York, NY, 10032, USA

[3] Integrated Program in Cellular, Molecular, and Biomedical Studies, Columbia University Irving Medical Center, New York, NY, 10032, USA

[4] Cambridge Institute for Medical Research, Department of Clinical Neurosciences, University of Cambridge, Cambridge CB2 0XY, UK

[5] Department of Chemical Engineering and Biotechnology, University of Cambridge, Philippa Fawcett Drive, CB3 0AS, Cambridge, UK

[6] Laboratory of Organic Chemistry, Stippeneng 4, 6703 WE, Wageningen University & Research, the Netherlands

[7] Department of Statistics, The University of Chicago, Chicago, IL, 60637, USA

[8] Department of Statistics, University of Pennsylvania, Philadelphia, PA, 19104, USA

[9] Center for Motor Neuron Biology and Disease, Columbia University Irving Medical Center, New York, NY, 10032, USA

[10] Department of Neurology, Eleanor and Lou Gehrig ALS Center, Columbia University Irving Medical Center, New York, NY, 10032, USA

[11] Physical Chemistry and Soft Matter, Stippeneng 4, 6703 WE, Wageningen University & Research, the Netherlands

[12] Department of Medicine, Division of Neurology, University Health Network and University of Toronto, Toronto, ON M5T 0S8, Canada.

[13] Department of Neurology, Taub Institute for Research on Alzheimer's Disease and the Aging Brain, Columbia University Irving Medical Center, New York, NY, 10032, USA

***Correspondence: ac4304@cumc.columbia.edu**

Abstract

Neurodegenerative disorders are a family of diseases that remain poorly treated despite their growing global health burden. A shared feature of many neurodegenerative disorders is the accumulation of toxic misfolded proteins. To gain insight into the mechanisms and modulators of protein misfolding, we developed a multiplex reverse genetics platform. Using this novel platform 29 cell-based models expressing proteins that undergo misfolding in neurodegeneration were probed against more than a thousand genetic modifiers. The resulting data provide insight into the nature of modifiers that act on multiple misfolded proteins as compared to those that show activity on only one. To illustrate the utility of this platform, we extensively characterized a potent hit from our screens, the human chaperone DNAJB6. We show that DNAJB6 is a general modifier of the toxicity and solubility of multiple amyotrophic lateral sclerosis and frontotemporal dementia (ALS/FTD)-linked RNA-binding proteins (RBPs), including FUS, TDP-43, and hnRNPA1. Biophysical examination of DNAJB6 demonstrated that it co-phase separates with, and alters the behavior of FUS containing condensates by locking them into a loose gel-like state which prevents their fibrilization. Domain mapping and a deep mutational scan of DNAJB6 support the critical importance for DNAJB6 phase separation in its effects on multiple RNA-binding proteins. Crucially, these studies also suggest that this property can be further tuned to generate novel variants with enhanced activity that might illuminate potential avenues for clinical translation.

Introduction

Human neurodegenerative diseases are a major source of morbidity and mortality worldwide and represent a significant unmet medical need[1-3]. A hallmark of many neurodegenerative diseases (NDDs) is the intracellular accumulation of misfolded protein aggregates[4,5]. To model the proteotoxicity imposed by NDD-associated proteins with an intrinsic propensity to aggregate such as Fused in Sarcoma (FUS), TAR DNA-binding protein (TDP-43), and alpha-synuclein, researchers have repeatedly turned to the yeast, *Saccharomyces cerevisiae*[6-8]. In yeast, expression of these aggregation-prone proteins results in slow growth. By screening for genes that restore growth upon overexpression, researchers have been able to identify pathways involved in modulating the underlying proteotoxicity, and validate their findings in lower throughput mammalian cell systems. As a whole, these screens have informed our understanding of disease pathobiology, and served as the basis for numerous therapeutic intervention strategies, some of which are being advanced by commercial entities[7-18].

While previous yeast-based studies have proven insightful, only a subset of NDD models have been screened. This likely reflects a systems-level limitation imposed by the significant effort involved in conducting large genetic screens. In addition, due to differences in the testing environment, genetic background, and method of screening, it is difficult to definitively compare results across studies in order to gain insight into broad versus narrow-acting regulators of proteotoxicity[7,8,18]. When comparisons between screens have been performed, few or no shared toxicity modifiers have been identified, even among related disease proteins such as TDP-43 and FUS[7,8,10]. This lack of correlation conflicts with overlaps in clinical presentation between TDP-43 and FUS patients and the shared biochemical and biophysical properties of both proteins[19]. Furthermore, as previous approaches are only able to study one model at a time, they have mainly focused on screening wild-type versions of NDD associated proteins, preventing our ability to assess if patient mutations alter the underlying molecular processes, which if found, would have significant implications in the treatment of this family of disorders[8,15]. Finally, most screens performed in yeast have searched for yeast genes that rescue the toxicity of NDD models, leading to identified hits with unclear or no known orthologous human counterpart to advance as a potential therapeutic candidate[8,10].

To overcome these limitations, we created a multiplex screening platform capable of simultaneously identifying genetic suppressors to 29 cell-based models expressing proteins that undergo misfolding in neurodegeneration. To interpret the wealth of data obtained, we built a custom analysis pipeline that prioritizes interactions for subsequent validation. Using this platform, we were able to identify previously elusive broadly-active rescuers, along with highly selective rescuers that only impact a single model. These studies revealed a plethora of genetic modifiers for future investigation, along with highlighting the diverse array of pathways and mechanisms that can potentially be exploited for therapeutic benefit.

84 Upon further examination of our results, we identified the human HSP40 co-chaperone, DNAJB6, as a potent
85 rescuer of the toxicity caused by the expression of multiple RNA-binding proteins associated with ALS/FTD.
86 Through subsequent studies in mammalian cells, we show that DNAJB6 has the ability to modulate the
87 solubility of FUS, TDP-43, and heterogeneous nuclear ribonucleoprotein A1 (hnRNPA1). We also use purified
88 proteins to demonstrate that DNAJB6 is able to phase separate and alter the liquid-liquid phase separation
89 properties of FUS. We show that DNAJB6 is able to maintain FUS in a loose gel-like state that prevents its
90 fibrilization over extending time periods. This mechanism is unique among modifiers of biologic condensates
91 and suggests an additional mechanism by which chaperones prevent the aggregation of clients. We
92 corroborate our *in vitro* findings by analyzing a series of truncation mutants and performing a deep mutational
93 scan within DNAJB6, along with suggesting mechanisms by which its activity can be further engineered.
94
95 **Results**
96 **Development of a multiplexed screening strategy to identify rescuers of proteotoxicity**
97 To enable our multiplex screening approach, we make use of isogenic yeast strains that each contain a unique
98 DNA-barcode inserted into a neutral genomic locus[20]. Into each of these barcoded strains, we deliver a
99 construct encoding a NDD-associated protein with a propensity to misfold (e.g., TDP-43, FUS, alpha-
100 synuclein). Growth of these strains in media that induces the overexpression of the toxic disease-associated
101 protein causes a reduction in cell growth, and provides a facile method of modeling the cellular dysfunction
102 elicited by these proteins. As each of our models (i.e. yeast expressing a unique protein of interest) are linked
103 to a particular DNA-barcode, we can combine them into a single mixed pool and track the growth of each
104 member by measuring its barcode abundance using next-generation sequencing. To identify novel regulators
105 of neurodegeneration, we probe the pool of disease models against a library of genetic modifiers (Sup. Fig.
106 1). In cases where a genetic modifier suppresses the toxicity of a particular NDD-associated protein, we
107 observe a marked increase in the abundance of the model's barcode as compared to the control condition
108 where the pool is exposed to an inert genetic modifier like mCherry. Taking advantage of the scalability
109 afforded by the use of DNA-barcoding, each examined protein is placed into several different DNA-barcoded
110 strains (i.e. redundant barcoding). This decreases assay noise by allowing us to use the collective behaviors
111 of all uniquely barcoded strains containing the same protein to derive our conclusions and enables us to
112 confidently identify significant interactions between our disease models and genetic modifiers[21].
113
114 To develop our approach, we analyzed multiple screening parameters such as strategies for pooling DNA-
115 barcoded strains based on their toxicity, appropriate number of experimental replicates, and the amount of
116 redundant barcoding required to detect interactions with high sensitivity (Sup. Note 1-3, Sup. Fig. 1-7). We
117 then assembled a collection of NDD-associated proteins based on previous publications (Fig. 1a and Sup.
118 Table 1)[13,22-24]. For a subset of these proteins, we also engineered a panel of point mutants based on familial
119 variants that increase the likelihood of disease to determine whether they might influence the observed rescue

120 (Fig. 1a). To assist in interpreting screening results, the final pool of cells was supplemented with a series
121 DNA-barcoded controls including cells that express a non-toxic fluorescent protein (mCherry), other
122 aggregation-prone proteins not associated with neurodegeneration (e.g. SUP35, RNQ1), or proteins linked to
123 neurodegeneration but which themselves are not prone to misfolding (e.g. ANG, OPTN). In total, our final
124 screening library contains 29 NDD-associated proteins plus multiple controls, each placed within 5-7 uniquely
125 DNA-barcoded strains all mixed together into a single pool for testing.
126
127 **Functional characterization of chaperone interactions with neurodegenerative disease models**
128 Using our final pool and optimized screening strategy, we probed a targeted library of 132 molecular
129 chaperones, 62 of which were from yeast and 70 from humans. Molecular chaperones have been previously
130 implicated in the refolding, turnover, and mitigation of the toxicity of aggregation-prone proteins associated
131 with neurodegeneration[5,25,26]. However, a comprehensive map of the functional interactions between
132 chaperones and their disease-associated clients remains elusive, limiting the field's ability to identify broadly-
133 active members of this class of proteins. We hypothesized that the approach described here would be uniquely
134 suited towards assessing this interaction space. In addition, it would also serve as a data-rich set to extensively
135 validate our methodology. Overall, this screen represents 5,850 genetic interactions between the various
136 proteotoxic models and controls and the corresponding library of molecular chaperones.
137
138 Within the yeast chaperone set, we observed 112 strong interactions that resulted in a greater than 0.5 log2
139 fold increase in barcode abundance (Fig. 1b, Sup. Fig. 8a, and Sup. Table 2). Notably, potentiated HSP104
140 chaperones were broadly active with the ability to rescue the proteotoxicity of a number of models including
141 two beta-amyloid models, hnRNPA1, and the dipeptide repeat PR50 associated with C9orf72 RAN-translation,
142 in addition to their previously reported rescue of TDP-43, FUS, and alpha-synuclein models[27]. Outside of
143 strong interactions, such as those observed with the HSP104 variants, 74 interactions with mild-to-moderate
144 positive log2 fold changes between 0.25 and 0.5 were also observed. In order to prioritize the 186 interactions
145 for further follow up, we developed an analysis pipeline to call interactions with statistically significant
146 enrichment (Fig. 1c, and Sup. Fig. 8b). This pipeline uses the control wells tested against inert rescuers (e.g.
147 mCherry) to develop an expectation for the abundance of each barcode in the pool, it then determines which
148 barcodes significantly increase in abundance in test wells, and combines information from barcodes
149 associated with the same model to identify the most potent and significant hits (see Materials and Methods
150 for details). Upon applying our data analysis pipeline, 100 interactions were called as significant (Sup. Table
151 2). Among these significant interactions, we identified specific interactions between the ALS/FTD-associated
152 RNA-binding proteins, EWSR1, FUS, and hnRNAP2B1 and the type I HSP40 chaperone YDJ1, the
153 chaperonin containing TCP-1 (CCT) subunit CCT6, and the small heat shock protein HSP42, respectively.
154 We also observed an interaction between the Golgi-maintenance protein and autophagosomal receptor OPTN

155 and a Rab family GTPase involved with ER-to-Golgi transport that localizes to pre-autophagosomal structures,
156 YPT1 (Fig. 1d).
157
158 The mammalian chaperone set contained 131 interactions that resulted in mild-to-moderate or strong log2
159 fold changes in barcode abundance (Fig. 1e and Sup. Fig. 9). However, 86 of the 131 interactions led to mild-
160 to-moderate changes in barcode abundance, possibly reflecting the suboptimal function of mammalian
161 chaperones within yeast cells (Fig. 1e and Sup. Fig. 9a). Nevertheless, 20 significant interactions were
162 identified, including rescue mediated by the primarily mitochondria-localized type III HSP40 chaperone,
163 DNAJC11, and two membrane associated proteotoxicity models, TMEM106B and Kar2-beta-amyloid (Fig. 1f-
164 g and Sup. Fig. 9b). These results are of interest as DNAJC11 mutant mice show prominent neuronal
165 pathology with vacuolization of the endoplasmic reticulum and disruption to mitochondrial membranes[28].
166 Furthermore, both TMEM106b and beta-amyloid cell-based models have been associated with mitochondrial
167 stress and dysfunction[23,29]. These findings suggest that the rescue with DNAJC11 may be related its ability to
168 buffer against the effects of amylogenic proteins on mitochondrial function. Given the breadth of our screening
169 it enabled the detection of a general trend of interaction between multiple human type II HSP40 chaperones
170 (DNAJB1, DNAJB2, DNAJB4, DNAJB6, DNAJB8) and two yeast prions, RNQ1 and SUP35 within our library.
171 These findings indicate that the misfolded intermediates produced by these two yeast prions may have similar
172 properties, which is in agreement with data showing the ability of these two yeast prions to cross-seed each
173 other's aggregation[30]. Furthermore, the fact that SIS1, the yeast orthologue of these human DNAJB proteins,
174 shows prominent activity against RNQ1 and SUP35, suggests that this class of misfolded prion species may
175 be evolutionarily conserved substrates for the DNAJB family of chaperones[31].
176
177 **Secondary validation of multiplexed screening results**
178 To validate the interactions identified in the screen, we applied a testing paradigm similar to how the screen
179 was conducted. For this purpose, we made use of a previously reported passaging-based growth assay, which
180 we first verified against a set of known interactions (Sup. Fig 10)[32]. We then used the assay to individually
181 validate two sets of hits, namely, those judged as statistically significant by our analytical pipeline and those
182 with positive log2 fold changes that did not reach our significance threshold but represent "suspected
183 interactions". Hits identified as statistically significant with an FDR adjusted p-value of <0.05 were validated at
184 a high rate, with 116/120 (96.7%) of these interactions reproducing upon individual testing (Sup. Table 3). We
185 next verified a number of suspected interactions with positive log2 fold changes that did not meet statistical
186 significance, with 59/95 (62.1%) of these suspected interactions showing rescue upon individual testing (Sup.
187 Table 3). This indicates that the hit-calling algorithm can prioritize interactions that are likely to validate over
188 using log2 fold changes alone, although some true hits may be missed as these likely do not survive our
189 adjustments for multiple hypothesis testing. To estimate the sensitivity and specificity of the statistical pipeline,
190 we assumed that the 175 validated interactions (116 significant and 59 suspected) represent most of the hits

191 in the matrix of 5,850 interactions. Holding this to be the case, it suggests that our screening platform has an
192 estimated sensitivity and specificity of ~66% and ~99%, respectively, which is on par or better than previously
193 reported one-model-at-a-time screening approaches[33-36]. Furthermore, highlighting the power of our
194 redundant barcoding strategy, if the number of barcodes analyzed for each model is progressively reduced
195 from 5-7 redundant barcodes per model to 1 per model, a striking decrease in the number of hits captured is
196 seen with each barcode removed (Sup. Fig. 11). These results reinforce the dramatic improvement in data
197 quality afforded by transforming each model into multiple DNA-barcoded strains and analyzing their collective
198 behavior.
199
200 To evaluate the performance of our platform against a larger, unbiased library of potential modifiers, we
201 screened the hORFeome V8.1 human cDNA library against our pool. We chose to screen human ORFs in
202 hopes of identifying hits that are more likely to directly translate to mammalian models of disease and because
203 of a paucity of prior reports of human genes being tested in this paradigm, suggesting that many novel
204 interactions likely remain to be uncovered. Screening ~900 members of the hORFeome library enabled the
205 examination of ~35,000 interactions, representing ~9 times more interactions surveyed within our system than
206 is typical[7,8,11,14,15]. Screening and subsequent validation of this collection of rescuers resulted in the
207 identification of 54 confirmed genetic interactions (Sup. Table 4, Sup. Table 5). As expected with a library
208 comprising random human genes, the occurrence of genetic interactions was significantly lower (0.14%)
209 compared to the curated molecular chaperone screen (2.9%). Furthermore, when compared to other unbiased
210 screens overexpressing yeast genes instead of human genes our hit rate remains lower (previously reported
211 hit rates of 0.24%-1.13% vs. 0.14%)[8,10,11,14]. One of the main drivers of this difference is likely the failure of
212 human genes to function in yeast cells, and further highlights the benefits of using a high-throughput
213 quantitative screening approach to rapidly explore this sparsely populated interaction space[37].
214
215 **DNAJB6 is a rescuer of multiple RNA-binding proteins implicated in ALS/FTD**
216 During screening and subsequent validation, we identified a human chaperone, DNAJB6 that rescued the
217 toxicity of cells expressing ALS/FTD-associated aggregation-prone RNA-binding proteins FUS, TDP-43, and
218 hnRNPA1 (Fig. 2a). DNAJB6 is a type II HSP40 co-chaperone expressed in a number of tissues, including
219 ubiquitously throughout the brain and spinal cord[38]. However, DNAJB6 expression is decreased in the brain
220 with aging potentially sensitizing neurons to misfolded protein stress[39,40]. HSP40 co-chaperones comprise a
221 large class of approximately 50 proteins in humans with an array of reported activities, but primarily function
222 by binding to misfolded proteins, trafficking them to HSP70 chaperones, and regulating protein-protein
223 interactions[41,42]. While DNAJB6 was the only type II HSP40 that was able to rescue TDP-43 toxicity, DNAJB1
224 and DNAJB2 could rescue the FUS and hnRNPA1 models, although their magnitude of rescue was 1/3 to 1/4
225 that of DNAJB6, suggesting DNAJB6 has properties that are unique among its family (Sup. Fig. 12). DNAJB6
226 has been previously shown to suppress the aggregation of polyglutamine repeat containing proteins[43-46]. In

227 addition, mutations in DNAJB6 cause Limb Girdle Muscular Dystrophy D1 (LGMDD1), in which affected
228 muscle tissue accumulates TDP-43 aggregates, suggesting it plays a role in the maintenance of TDP-43
229 solubility within humans[47,48]. Nonetheless, it remains unclear as to whether DNAJB6 is a broadly active
230 modifier of other disease relevant clients and how DNAJB6 modulates misfolding[49,50].
231
232 In order to determine if the interaction between DNAJB6 and the RNA-binding proteins FUS, TDP-43, and
233 hnRNPA1 are relevant within mammalian cell contexts, we employed an *in vivo* protein aggregation assay[49,51].
234 In this assay, when FUS, TDP-43, or hnRNPA1 are overexpressed within human embryonic kidney 293T
235 (HEK293T) cells, they form SDS-insoluble species (RIPA buffer insoluble), that can be solubilized in urea. As
236 compared to control cells co-transfected with enhanced yellow fluorescent protein (EYFP), cells co-transfected
237 with DNAJB6 showed a reduction in the amount of SDS-insoluble FUS, TDP-43, and hnRNPA1 (Fig. 2b-e).
238 This result demonstrates that DNAJB6 can reduce the formation of insoluble species for multiple RNA-binding
239 proteins within mammalian cells.
240
241 **Endogenous DNAJB6 participates in the response to accumulation of insoluble FUS, TDP-43, and**
242 **hnRNPA1**
243 To further investigate the mechanisms and role DNAJB6 plays in the response to increasing cellular
244 concentration of ALS/FTD-associated RNA-binding proteins, we transfected HEK293T cells with EYFP, FUS,
245 or TDP-43 expression constructs and performed unbiased RNA-sequencing. As compared to the EYFP
246 control condition, DNAJB6 was amongst the most strongly and significantly upregulated chaperones within
247 the ~270 molecular chaperones observed upon overexpression of FUS and TDP-43 (Sup. Fig. 13).
248
249 To determine what role endogenous levels of DNAJB6 play in regulating FUS, TDP-43 and hnRNPA1
250 misfolding, Cas9 was used to generate multiple independent clones in which DNAJB6 was knocked out (Fig.
251 2f). In DNAJB6 knockout lines, SDS-insoluble FUS, TDP-43, or hnRNPA1 species were not observed when
252 these proteins were expressed at endogenous levels (Sup. Fig. 14). However, upon overexpression of FUS,
253 TDP-43, or hnRNPA1, greater amounts of SDS-insoluble species within DNAJB6 knockout lines were
254 observed compared to the non-targeting gRNA control (NTC) lines (Fig. 2g-j).
255
256 Taken together, these data suggest that DNAJB6 is part of a programmed cellular response to rising levels of
257 multiple aggregation-prone RNA-binding proteins and that physiological levels of DNAJB6 can regulate the
258 solubility of these proteins.
259
260 **DNAJB6 undergoes phase separation and can prevent aberrant FUS interactions *in vitro***
261 The amino acid sequence of DNAJB6 contains multiple stretches of low complexity residues, which is a feature
262 of many proteins that undergo liquid liquid phase separation (LLPS). This, together with the fact that DNAJB6

263 interacts with and rescues the aggregation of multiple proteins that undergo LLPS in cells (e.g. FUS, TDP-
264 43), prompted us to investigate whether DNAJB6 might itself undergo LLPS[52-54]. To address this question, we
265 deployed a previously published LLPS assay[51,55]. Incubation of DNAJB6 (3 μM or 0.25 μM) in near
266 physiological salt concentrations (50 mM NaCl) resulted in phase separation and formation of liquid liquid
267 droplets of DNAJB6 (Sup. Fig. 15a-b)[56].
268
269 This experimental result raises the question as to whether DNAJB6 might co-partition with its phase separating
270 client proteins such as FUS. To address this question, we mixed FUS and DNAJB6 at intracellular
271 concentrations determined from the literature (1.5 μM and 0.25 μM respectively) in near physiological NaCl
272 concentrations (50 mM)[57]. Under these experimental conditions, as well as at a 1:1 molecular ratio, (not
273 shown) DNAJB6 and FUS co-partitioned into the condensed liquid droplet phase (Sup. Fig. 15c). Intriguingly
274 however, the FUS + DNAJB6 condensates were more numerous, and had noticeably smaller diameters than
275 FUS only condensates, suggesting that binding of DNAJB6 to FUS might modulate FUS-FUS interactions,
276 thereby preventing FUS condensate progression and growth (Fig. 3a-b). If correct, this might also provide a
277 mechanism through which DNAJB6 might modulate the propensity of FUS to undergo time-dependent
278 progressive condensation ("aging") into fibrillary aggregates[51,54,58].
279
280 To further characterize the effect of DNAJB6 on FUS condensation across different timescales, we employed
281 four orthogonal assays of the biophysical state of FUS – direct inspection of droplet morphology and fibrillary
282 aggregates, fluorescence lifetime imaging microscopy (FLIM), fluorescence recovery after photobleaching
283 (FRAP), and atomic force microscopy with infrared nanospectroscopy (AFM-IR). The direct inspection of the
284 FUS condensates over time reveal that FUS + DNAJB6 condensates remain small and spherical, with no
285 irregular fibrillary aggregates. In contrast, the FUS only condensates form large spherical condensates, which
286 by 36 hours are accompanied by occasional fibrillary aggregates (Fig. 3c).
287
288 These results suggest that DNAJB6 constrains FUS condensation and prevents fibrillary aggregation. In
289 addition, the persistently small size of the FUS + DNAJB6 condensates is consistent with the formation of a
290 loose gel-like state which inhibits droplet droplet fusion events (Ostwald Ripening) that are characteristic of
291 pure liquid liquid droplets. The FLIM assays, which measure the local packing environment showed a
292 significant increase in FLIM lifetimes of FUS within FUS + DNAJB6 condensates at all time points from 20
293 minutes to 48 hours after condensate formation compared to the FUS only control (Fig. 3d). This result
294 suggests that DNAJB6 permits FUS condensation to occur, but limits FUS-FUS packing and further
295 condensation. In good agreement with this conclusion, the FRAP experiments at 30 minutes, revealed
296 increased FRAP recovery rates in FUS + DNAJB6 condensates (Sup. Fig. 15d). However, at 24 hours, both
297 the larger FUS only condensates and the smaller FUS + DNAJB6 condensates showed little FRAP recovery
298 (data not shown). This likely reflects further condensation of FUS in both condensate types, albeit with

299 potentially different condensation states in the FUS only versus the FUS + DNAJB6 condensates at these
300 later time points that are not discriminable by FRAP.
301
302 The morphological analysis of condensate size, together with the FLIM and FRAP data suggest that the
303 FUS + DNAJB6 condensates may form spherical, loosely condensed gel-like structures. In contrast, FUS-
304 only condensates tended to form more compact condensates with a propensity to form fibrillar aggregates.
305
306 To interrogate the nature of the spherical condensates in the FUS-only and the FUS + DNAJB6 conditions,
307 we applied atomic force nano infrared spectroscopy as described previously[51,55]. Studies of individual
308 spherical condensates on zinc selenide chips revealed that spherical FUS + DNAJB6 condensates
309 contained higher content of intermolecular parallel β-sheet and less content of intermolecular antiparallel β-
310 sheet than the spherical FUS-only droplets (Fig. 3e-f and Sup. Fig 16). Furthermore, the parallel β-sheet of
311 FUS + DNAJB6 shifted at a lower wavenumber, indicating more extended strands and more hydrogen
312 bonding. These spectral properties have previously been associated with gelled polymers and therefore
313 support the hypothesis that DNAJB6 prevents progression of FUS condensation into irreversible fibrillary
314 aggregates by incorporating them into looser gel-like condensates[55,59-64].
315
316 **Characterization of DNAJB6 via domain deletions and deep mutational scanning**
317 Having established the ability of DNAJB6 to phase separate and directly interact with its clients to prevent
318 their misfolding, we sought to decipher the regions within the protein required for its effect within cells. A series
319 of DNAJB6 deletion mutants were constructed, including versions lacking the J-domain which is necessary
320 for activation of HSP70 partners, the glycine/phenylalanine rich region which contributes to its ability to phase
321 separate, and the serine rich domain that is implicated in client recognition and binding[43,45]. Deletion of any of
322 these domains prevented DNAJB6 from rescuing FUS toxicity within yeast, consistent with the recent results
323 using purified proteins for a related HSP40 chaperone, DNAJB1, and its interaction with FUS (Sup. Fig. 17a)[65].
324 All the examined deletion mutants were expressed in yeast except for the variant with the J-domain removed.
325 To better examine the role for the J-domain a point mutant within the conserved HPD motif of the J-domain
326 (H31Q) was created. This mutant expresses well but blocks the ability of DNAJB6 to stimulate the ATPase
327 activity of HSP70 family members[42]. The H31Q mutation also rendered DNAJB6 non-functional for rescuing
328 FUS-mediated toxicity. These results suggest that all domains within DNAJB6 are required for its activity and
329 that cooperating with a HSP70 partner may be necessary for its full function *in vivo* (Sup. Fig. 17a-b).
330
331 During our deletion analysis, we observed that loss of the glycine/phenylalanine (G/F) rich domain or the
332 serine (S) rich domain from DNAJB6 enhanced the toxicity of the FUS model (Sup. Fig. 17b). These regions
333 have been implicated in substrate recognition and are also the site of mutation within LGMDD1 patients along
334 with multiple variants of uncertain significance within the ClinVar database. To decipher the function of this

335 critical region at increased resolution, we conducted a deep mutational scan (DMS) across the 112 amino
336 acids of the G/F and S-rich regions. Deep mutational scanning libraries were constructed by performing
337 comprehensive mutagenesis of each codon, yielding versions of DNAJB6 with all possible amino acids or a
338 stop codon at each interrogated position (Fig. 4a). The library of variants was then tested for their ability to
339 rescue the proteotoxicity induced upon FUS overexpression, creating a comprehensive fitness landscape of
340 all single amino acid mutations in the G/F and S rich region on DNAJB6 activity (Fig. 4b). Mutagenesis libraries
341 were constructed and screened in biological duplicates, with strong correlation between replicates observed
342 (see Materials and Methods, Sup. Fig. 18). Notably, regions rich in patient mutations causing LGMDD1 (amino
343 acids 89-100) frequently resulted in a reduction in activity, with subsequent validation of these mutations
344 confirming a loss of activity compared to wild-type (WT) DNAJB6 against the FUS model (Fig. 4b-c). Similar
345 results were obtained when these mutants were tested against the TDP-43 model, in agreement with the
346 existence of a common mechanism of interaction between DNAJB6 and its aggregation-prone clients (Fig.
347 4c). Numerous variants of uncertain significance (VUS) in DNAJB6 present in ClinVar were also captured
348 within the data. Follow-up studies individually examining these mutants revealed a subset which were
349 defective in their ability to rescue FUS and TDP-43 expressing models, suggesting that additional disease
350 associated mutants may exist outside what is currently annotated (Fig. 4c). Within the DNAJB6 mutational
351 landscape, variants with enhanced activity against FUS were observed. Outside of the conservative S192T
352 mutation which showed one of the strongest effects on rescue, a general trend was seen where mutation to
353 an acidic residue in stretches between 138-171 and 182-189 appeared to enhance activity compared to WT
354 DNAJB6 (Fig. 4b). In line with this observation, the single acidic amino acid within these stretches, D158, was
355 critical for function as mutation of D158 to almost any other amino acid other than glutamic acid reduced the
356 activity of the protein (Fig. 4b). Based on the screening results, several DNAJB6 mutants with enhanced
357 activity were selected for validation against both the FUS and TDP-43 models within yeast, revealing 3
358 mutations that showed clear gains in activity as compared to the wild-type protein (Fig. 4c).
359
360 To further establish the relevance of the enhanced DNAJB6 variants, their ability to reduce the formation of
361 SDS-insoluble, urea-soluble FUS species in mammalian HEK293T cells was examined. Given that WT
362 DNAJB6 almost entirely reduced the formation of SDS-insoluble, urea-soluble FUS, the assay was modified
363 by transfecting more FUS expression plasmid into cells which resulted in higher levels of SDS-insoluble, urea-
364 soluble FUS species (Sup. Fig. 19). Utilizing higher FUS expression, the potentiated DNAJB6 variants, G182E
365 and S192T showed a further reduction in the formation of SDS-insoluble, urea-soluble FUS species as
366 compared to the wild-type protein (Fig. 4d-e). These findings demonstrate that the activity of DNAJB6 can be
367 further improved and that rescuer proteins optimized in yeast can be readily translated to mammalian cell
368 systems[27].
369
370 **Discussion**

371 Modeling of neurodegeneration in simplified cellular systems has yielded insights into how proteotoxic
372 aggregation-prone proteins disrupt cellular function. However, a great deal of additional information is required
373 to fully understand these complex processes, and provide practical information that can be translated into
374 effective diagnostics and therapeutics for the associated human medical disorders. The work described here
375 advances this goal in two ways. First, we developed a multiplexed approach in which numerous misfolding-
376 prone proteins can be screened in parallel to identify a rich dataset of candidate modulators acting either in a
377 protein-specific way, or in a more general class-specific way. Second, our work has uncovered a previously
378 unrecognized mechanism whereby protein:protein interactions can modulate the propensity of misfolding-
379 prone proteins to form species that injure cells - namely by the formation of gel-like biomolecular condensates
380 instead of irreversible fibrillar condensates. In the paragraphs below, we explore each of these concepts in
381 greater detail.
382
383 *A novel platform for identifying modulators of proteotoxic protein misfolding*
384 Our platform provides several advantages over conventional approaches. Specifically, by inserting the same
385 misfolding-prone protein into several uniquely barcoded strains and by analyzing their collective response to
386 a given genetic perturbation, we are able to greatly enhance our assay sensitivity and specificity. Crucially,
387 the quantitative nature of our approach better enables us to capture mild changes in growth by a putative
388 rescuer as compared to traditional semi-quantitative methods. Moreover, by simultaneously studying multiple
389 models within the same genetic background and under the same testing paradigm, we are able to make broad
390 observations about the nature of rescuers and the relationship between models. Finally, in contrast to previous
391 studies that screen cDNA libraries derived from the model organism being used (e.g. yeast or flies), we
392 demonstrate across dozens of models that our platform enables direct screening of human genes within simple
393 organisms such as yeast to identify disease relevant suppressors. Overall, this work establishes a high-
394 throughput platform for identifying novel genetic suppressors applicable to any family of proteins so long as
395 their expression in yeast causes a growth defect that is dependent upon the biological function the user desires
396 to interrogate[66,67]. Furthermore, with minor modifications our approach can be readily applied toward
397 screening against libraries of small molecules to identify compounds with specific versus broad activities
398 against classes of disease relevant proteins such as the NDD-associated proteins studied in this work.
399
400 An additional finding from our screens was the lack of concordance between proteotoxic species of the same
401 class, such as various dipeptide repeats and poly-alanine models. In contrast, RNA-binding proteins showed
402 a general trend for having rescuers that were active on several members of its group. No rescuers, however,
403 showed clear activity on all RNA-binding proteins and each tended to show a preference for a particular subset
404 (Fig. 2 and Sup. Fig. 8-9). These results imply that there is no universal feature that is conserved across a
405 given family of NDD-associated proteins, but that there can still be some areas of conserved identity among
406 the misfolded species that enable genetic modifiers to interact with several members of the family.

407

408 As our library also contained variants of the same protein of interest with different patient mutations, we asked
409 what, if any, was the effect of these mutations on our screening results. Interestingly, despite many of the
410 tested mutations having been shown to accelerate the rate of protein misfolding or drastically alter the
411 localization of the variant protein, they appeared to be rescued in a similar manner as the wild-type protein
412 (Sup. Fig. 8-9)[51,54,68,69]. These results suggest that the tested patient mutations, while increasing the probability
413 of misfolding (and thus probability of disease), do not appear to fundamentally change the underlying
414 mechanism of toxicity or the misfolded state that is present within the cell. These results raise the possibility
415 that a therapeutic modality designed against the wild-type form of a protein might also work for patients with
416 rare disease-causing variants.

417

418 *Changing the phase state of phase separating proteins forming biomolecular condensates*

419 The work reported here has revealed that certain chaperone proteins (e.g. DNAJB6) can interact with phase
420 separating RNA binding proteins (e.g. FUS, TDP-43, hnRNPA1). Prior work has shown that these RNA binding
421 proteins form reversible biomolecular condensates that are crucial to their function in nuclear RNA
422 transcription, and particularly in cytoplasmic RNA translation in selected vulnerable niches such as axon
423 terminals of neurons[51,55,70-72]. However, these biomolecular condensates, even when comprised of wild-type
424 RNA binding proteins, have a propensity to condense into irreversible assemblies enriched in β-sheet
425 fibrils[51,54,58]. The formation of these irreversibly condensed assemblies inhibits the function of the RNA binding
426 proteins in RNA transcription and RNA translation. This latter effect reduces new protein synthesis in axon
427 terminals, which are particularly dependent upon local RNA translation for the production of niche-specific
428 proteins involved in synaptic viability and function[51,55,70-72].

429

430 Our data shows that DNAJB6 co-fractionates with FUS under near physiological conditions, and encourages
431 the formation of less compact, gel-like condensates, thereby preventing the formation of irreversible fibrillar
432 aggregated species. This finding is in contrast to other identified rescuers of FUS misfolding, such as TNPO1,
433 which deters FUS aggregation by dissolving condensates[55].

434

435 Additional work will now be required to probe if and how chaperone-induced formation of gel-like condensates
436 might still allow effective local RNA translation in neurons. For instance, do the chaperone-induced gel-like
437 condensates act like a percolated gel, and permit release of naked RNA species for access by local RNA
438 translation machinery? Alternatively, are the chaperone-induced gel-like condensates simply being held in a
439 phase state that is still reversible, perhaps through interactions with other local chaperones and
440 disaggregases, converting them back to more liquid-like assemblies? In this latter regard, while our work has
441 focused primarily on DNAJB6, HSP40 family members often work in concert with HSP70 chaperones, which
442 are also known to regulate the solubility of ALS/FTD-associated RNA-binding proteins[73]. In future studies,

443 modeling *in vitro* the behavior of DNAJB6 with a HSP70 partner could reveal additional insights into the
444 process by which it helps maintain aggregation-prone proteins such as FUS soluble *in vivo*.
445
446 Finally, it is important not to overlook prior work which has demonstrated that DNAJB6 can prevent the
447 aggregation of poly-glutamine repeat expansion containing proteins, along with acting on beta-amyloid and
448 alpha-synuclein[39,43,44,46,74,75]. Taken together with our study, these results raise the possibility that DNAJB6
449 represents a generalized chaperone for a number of clinically relevant misfolded species. Furthermore, the
450 ability to observe DNAJB6 activity in an easy to manipulate yeast model enables the high-throughput
451 optimization of its activity. We demonstrate that extensive deep mutational scanning of DNAJB6 can identify
452 enhanced variants. Additional screening of these mutant libraries against numerous protein misfolding models
453 could be used to select for more broadly-active versions of the protein. Alternatively, these same mutant
454 libraries could be used to selectively tune DNAJB6 towards a narrower class of targets should an increase in
455 specificity be desired for eventual therapeutic applications. By examining, the properties and three-
456 dimensional structure of the obtained enhanced DNAJB6 proteins, we can gain fundamental insights into how
457 these classes of proteins may function and evolve, along with informing future gene based therapies or the
458 design of small molecules that activate DNAJB6 function or mimic its activity.

459 **Materials and Methods**

460 **Yeast Strains and Media**

461 Barcoded *S. cerevisiae* yeast BY4741 *MATa his3Δ1 leu2Δ0 ura3Δ0 met15Δ0* strains were purchased from
462 Horizon (Cat. #YSC5117). To introduce rescuers through mating, rescuer containing *S. cerevisiae* yeast
463 BY4742 strains *MATα his3Δ1 leu2Δ0 ura3Δ0 lys2Δ0* were used. Individual barcoded strains containing
464 expression vectors were maintained in Synthetic Complete (SC) -ura media (20 g/L glucose, 1.5 g/L Drop Out
465 mix [US Biological D0539-09A], 1.7 g/L Yeast Nitrogen Base [US Biological Y2030], 5 g/L Ammonium Sulfate
466 [Fisher H8N2O45], supplemented with 18 mg/L Leucine and 9 mg/L Histidine). Individual rescuer BY4742
467 strains were maintained in SC -his media (20 g/L glucose, 1.5 g/L Drop Out mix [US Biological D0539-09A],
468 1.7 g/L Yeast Nitrogen Base [US Biological Y2030], 5 g/L Ammonium Sulfate [Fisher H8N2O45],
469 supplemented with 18 mg/L Leucine and 1.8 mg/L Uracil). Mating was conducted in YPD media (20 g/L
470 glucose, 20 g/L peptone, and 10 g/L yeast extract). Selection for mated strains was conducted in SC -ura -his
471 media (20 g/L glucose, 1.5 g/L Drop Out mix [US Biological D0539-09A], 1.7 g/L Yeast Nitrogen Base [US
472 Biological Y2030], 5 g/L Ammonium Sulfate [Fisher H8N2O45], supplemented with 18 mg/L Leucine), while
473 outgrowth of induced mated strains was carried out in SC -ura -his gal media (20 g/L galactose, 1.5 g/L Drop
474 Out mix [US Biological D0539-09A], 1.7 g/L Yeast Nitrogen Base [US Biological Y2030], 5 g/L Ammonium
475 Sulfate [Fisher H8N2O45], supplemented with 18 mg/L Leucine)

476

477 **Plasmids**

478 Proteotoxic genes and controls were cloned into either the pAG416GAL-ccdb (Addgene #14147) or
479 pAG426GAL-ccdb (Addgene #14155) using Gateway LR II Clonase Enzyme mix (Invitrogen). Once
480 expression plasmids were sequence verified, they were transformed into barcoded BY4741 strains using
481 standard LiOAc transformation protocols and plated on SC -ura agar plates. Yeast rescuer genes and control
482 rescuer genes were cloned into pAG413GAL-ccdb (addgene #14141) using Gateway cloning. Human rescuer
483 genes from the hOrfeome V8.1 Library collection were cloned into a derivative of pAG413GAL-ccdb,
484 pAG413GAL-ccdb-6Stop, wherein the 3' attR2 site was modified to encode a stop codon 6 amino acids
485 downstream of the last codon to compensate for a lack of a stop codon in the ORFeome.

486

487 All mammalian expression vectors were cloned into the pLEX307 backbone (Addgene #41392) using Gateway
488 LR II Clonase Enzyme mix (Invitrogen).

489

490 Plasmid DNA was isolated using standard miniprep buffers (Omega Biotek) and silica membrane columns
491 (Biobasic). All expression plasmids were Sanger sequenced to confirm the appropriate insert (Genewiz).

492

493 **Yeast Multiplexed Screening**

494 Each plate of rescuers was screened in biological duplicates. A fresh aliquot (500 µL) of frozen barcoded
495 yeast pool was inoculated into 5 mL of SC -ura media and rotated at 30°C. At the same time, 5 µL of each
496 rescuer strain was inoculated into 500 µL of SC -his media in 96 well 2 mL deep well plate format (VWR) and
497 shaken at 900 rpm at 30°C. 24 h later, 5 µL of the saturated barcoded yeast pool was mixed individually with
498 5 µL of rescuer strain in a new 96 well plate where each well was filled with 500 µL of YPD and shaken at 900
499 rpm at 30°C. For selection of mated strains, 20 h later, 5 µL of mated barcoded yeast pool was transferred
500 into a new 2 mL deep well plate filled with 500 µL of SC -ura -his media and shaken at 900 rpm at 30°C for 24
501 h. For outgrowth, 2 µL of the mated and selected pool was inoculated into 1 mL of SC -ura -his galactose
502 media and shaken at 1,000 rpm at 30°C for 30 h.
503
504 After growth, 100 µL of yeast culture was removed and the optical density (OD595) of the culture was
505 determined in a 96 well plate reader (Tecan). After measurement of culture density, genomic DNA was
506 extracted using a modified LiOAc-SDS extraction method. Briefly, plates were centrifuged for 5 min at 4,000
507 rpm. Supernatant was discarded and the pellet was resuspended in 200 µL of 200 mM LiOAc with 1% SDS
508 with rigorous pipetting. Plates were sealed with aluminum foil and incubated at 70°C for 20 min to enable lysis.
509 600 µL 100% ethanol was added to each well and pipetted up and down rigorously before being centrifuged
510 for 10 min at 4,000 rpm. Supernatant was discarded and pellets were air dried for 30 min under flame. Pellets
511 were then resuspended in 200 µL 1X TE and incubated at 42°C for 30 min. The plates were centrifuged for
512 10 min at 4,000 rpm and the supernatant containing DNA was pipetted into a new plate for storage at -20°C.
513 Raw sequencing reads from the chaperone screen have been uploaded to the NCBI SRA under BioProject
514 PRJNA769721 (SUB10508463). Raw sequencing reads from the orfeome screen have been uploaded to the
515 NCBI SRA under BioProject PRJNA769721 (SUB10508562).
516
517 **Sequencing Library Preparation**
518 For sequencing on NextSeq 500/550 (Illumina), libraries were prepared from genomic DNA in two PCR steps.
519 The first step amplifies genomic DNA containing the DNA barcode and attaches an internal index to designate
520 which column the well was amplified from. The second PCR attaches Illumina indexes to the amplicon,
521 wherein the combination of Illumina indexes indicates the row and plate location of the well. The first PCR
522 step was done in technical duplicates unless otherwise stated with Taq polymerase (Enzymatics). The
523 following reaction mix was used: 2 µL 10X Taq buffer, 0.1 µL 100 µM forward primer, 0.1 µL 100 µM reverse
524 primer, 0.1 µL Taq polymerase, 0.4 µL 10 mM dNTPs, 0.5 µL DNA, and 16.8 µL H_2O. The following cycling
525 conditions were used: 1. 94°C, 180 s, 2. 94°C, 30 s, 3. 60°C, 20 s, 4. 72°C, 30 s, 5. Return to step 2 27X, 6.
526 72°C, 180 s. After the first round of PCR, technical replicates of each individual well were pooled. For the
527 second round of PCR where Illumina indexes were attached, the following reaction mix was used: 2 µL 10X
528 Taq buffer, 0.1 µL 100 µM forward primer, 0.1 µL 100 µM reverse primer, 0.1 µL Taq polymerase, 0.4 µL 10
529 mM dNTPs, 0.5 µL DNA from first round PCR, and 16.8 µL H_2O. The following cycling conditions were used:

530 1. 94°C, 180 s, 2. 94°C, 30 s, 3. 56°C, 20 s, 4. 72°C, 30 s, 5. Return to step 2 7X, 6. 72°C, 180 s. After the
531 second round PCR, all reactions corresponding to a plate of screening were pooled together. The reaction
532 products were run out on a gel and a band corresponding to the right size was gel extracted. Libraries were
533 quantified with the NEBNext Library Quant Kit for Illumina according to manufacturer instructions (NEB).
534 Pooled libraries were combined and sequenced with a 75 cycles NextSeq 500/550 High Output Kit on a
535 NextSeq 500/550 machine (Illumina).
536
537 **Analysis of Multiplexed Screening**
538 Raw reads in fastq format were trimmed and assigned to wells via combinations of Illumina indexes and
539 column designating internal indexes. 20 bp barcode sequences were aligned to a reference genome allowing
540 for +1 or -1 shifts in the sequencing phase using bowtie2. Raw counts of exact matches for each barcode
541 were determined and well-read counts were normalized by the total number of reads in that well and converted
542 to counts per million (CPM) unless otherwise stated. Wells were analyzed in batches with other wells in the
543 same plate. Wells with less than 15,000 total reads were discarded in addition to wells where 1 biological
544 replicated received less than 15,000 total reads. After CPM normalization, the estimated actual abundance of
545 reads were calculated by normalizing against the optical density (OD595) of that well, which was measured
546 immediately prior to harvesting with a 96 well Infinite F50 plate reader (Tecan). Wells containing control or
547 inert rescuers were identified and the average read counts of each barcode in controls was determined. The
548 variance in the number of reads between control wells for each barcode was determined. The mean-variance
549 relationship was modeled using the equation log(σvariance-mean) = log(k)+b*log(mean)σ as previously
550 described[76]. The barcode mean and adjusted variance were used to determine whether a barcode in a test
551 well was significantly upregulated using a one-sided cumulative density function assuming a normal
552 distribution. The associated p-value was adjusted using a Benjamini-Hochberg procedure correcting for the
553 number of tests in that well. To obtain model level information from individual barcode strains, p-values from
554 independent barcode strains associated with the same model were combined using Stouffer's method. After
555 this summary value was obtained, a further Benjamini-Hochberg procedure was used to correct summary
556 values for the number of models and the number of wells in each plate. Average log2 fold change was
557 calculated as the base 2 logarithm of the average change in counts over the expected value in the control
558 wells. Analysis was conducted with custom scripts in R Version 4.0.2.
559
560 **Spot Assays**
561 Yeast strains to be assayed were grown overnight in selective synthetic complete media until saturation was
562 reached. Saturated cultures were serially diluted 1:5 in sterile PBS (Gibco). To SC –ura -his glucose or
563 galactose agar plates, 5 µL of diluted culture was spotted. Plates were left for 30 minutes to dry before being
564 inverted and incubated at 30°C for 48 h, followed by being scanned to document growth.
565

566 **Yeast Liquid Culture Growth Assay**

567 Proteotoxic yeast strains were grown in 500 µL SC -ura media in plate format shaken at 1,000 rpm at 30°C
568 for 24 h. At the same time, rescuer yeast strains were grown in 500 µL SC -his media shaken at 1,000 rpm at
569 30°C for 24 h. After growth, 5 µL of appropriate proteotoxic and rescuer yeast strains were mixed in 500 µL
570 YPD and shaken at 1,000 rpm at 30°C for 24 h. To 500 µL of dual selective SC -ura -his media, 5 µL of mated
571 strains were inoculated and shaken at 1,000 rpm at 30°C for 30 h. 48 h prior to reading, mated and selected
572 strains were inoculated in SC -ura -his galactose media at one of 3 dilution factors (Sup. Table 1) depending
573 on their growth rate and shaken at 1,000 rpm at 30°C for 24 h. 24 h after initial inoculation, strains were
574 passaged depending on their specified dilution factor into fresh SC -ura -his galactose media. Upon reaching
575 the assay endpoint, 100 µL of each well was transferred to a 96 well plate (Greiner) and the optical density
576 was determined on a 96 well plate reader (Tecan). Multiple media only wells were also quantified as a baseline
577 and these values were subtracted from optical density measurements. All statistics were performed in
578 GraphPad Prism Version 9.2.0.

579

580 **Protein Harvesting and Western Blotting**

581 *RIPA/Urea Extractions:* Cells in 24-well dishes were washed with ice cold PBS (Gibco) after media was
582 removed. 250 µL of RIPA buffer (50mM Tris-HCl (pH 7.4), 150mM NaCl 1% NP-40, 0.5% sodium deoxycholate
583 and 0.1% SDS, Alfa Aesar) was added to each well and allowed to sit for 2 min. Cells were resuspended in
584 RIPA buffer and moved to conical tubes. To lyse cells further, cells were sonicated for 10 s while kept on ice.
585 Cell lysate was centrifuged for 20 min at 12,000 x g at 4°C and supernatant was saved as RIPA soluble
586 fraction. Pellets were washed 1X with RIPA buffer and 50 µL urea buffer was added (8M Urea, 2M Thiourea,
587 4% CHAPS,) with vigorous pipetting to resuspend pellet and spun for 20 min at 12,000 x g at 4°C. The
588 concentration of protein in the RIPA buffer was determined with a Bradford assay and lysates were adjusted
589 to a final concentration between 250-350 µg/µL depending on the yield of the lowest concentration of the
590 lysate in the set in which it was processed with 1X LDS loading buffer (Invitrogen). RIPA soluble fractions
591 were boiled for 5 minutes and stored at -80°C until use. Urea fractions were stored at -80°C without boiling.

592

593 *Yeast Lysate Extraction:* Cells were collected and centrifuged at 2,300 x g for 2 min and washed with 1 mL of
594 dH_2O. To pelleted yeast cells, 200 µL of 0.1M NaOH was added and cells were resuspended by vortexing.
595 Cells were allowed to lyse for 10 min at room temperature. Lysed cells were spun at 13,000 x g for 1 min and
596 supernatant was discarded. Pellets were resuspended in 50 µL of dH_2O and 25 µL of 200 mM DTT (Fisher)
597 was added along with 25 µL of 4x LDS loading buffer (Invitrogen). Samples were boiled at 95°C for 5 min and
598 subsequently centrifuged at 800 x g for 10 min at 4°C. Supernatants were collected and moved to a new tube
599 for storage at -20°C.

600

601 *Western Blotting:* 10 µL of normalized lysate with loading buffer was loaded into NuPAGE 4 to 12% Bis-Tris
602 protein gels (Invitrogen) and subjected to 100 V electrophoresis for 65 min. Separated proteins were
603 transferred onto a 0.2 µM PVDF membrane and blocked with SuperBlock (Invitrogen). Primary antibodies
604 were diluted in SuperBlock with 0.1% Tween-20 and incubated overnight at 4°C with gentle rotation. Blots
605 were washed with TBST before secondary antibody incubation. Blots were imaged with the Odyssey XF
606 imaging system (Li-Cor) using the chemiluminescent detection. After transfer, blots were stained with Ponceau
607 S stain (G Biosciences) for 15 min. Total protein was imaged on a LAS-4000 imager (Fujifilm). Band intensities
608 were quantified with Image Studio Lite (Li-Cor).
609
610 TDP-43 was detected with a polyclonal rabbit antibody at a 1:2,500 dilution (Proteintech 10782-2-AP). FUS
611 was detected with a polyclonal rabbit antibody at a 1:2,500 dilution (Proteintech 11570-1-AP). hnRNPA1 was
612 detected with a polyclonal rabbit antibody at a 1:5,000 dilution (Proteintech 11176-1-AP). DNAJB6 was
613 detected with a monoclonal mouse antibody at a 1:2,500 dilution (Proteintech 66587-1-Ig). A goat anti-rabbit
614 HRP conjugated antibody was used at a 1:50,000 dilution (Invitrogen G21234). A goat anti-mouse HRP
615 conjugated antibody was used at a 1:10,000 dilution (Invitrogen 31430). All statistics were performed in
616 GraphPad Prism Version 9.2.0.
617
618 **Protein purification and *in vitro* LLPS experiments**
619 FUS-mEmerald was purified as previously described[55]. His-Sumo tagged DNAJB6 expression vector was
620 transformed into *E. coli* BL21(DE3) (NEB) for protein expression and purification. DNAJB6 expressing cells
621 were grown at 37°C until an OD600 of 0.6 was reached. Expression was induced with 0.5 mM IPTG overnight
622 at 16°C. Cell pellets were collected and subjected to high pressure lysis (Constant System) in lysis buffer (50
623 mMTris pH 7.5, 20 mM imidazole, 500 mM NaCl with 1x protease inhibitor cocktail). Lysate was centrifuged
624 at 100,000 x g and collected supernatant was applied to a 10 mL Ni-Advance (BioServ, UK) column. After
625 washing, His-Sumo tagged DNAJB6 was eluted in 250 mM imidazole containing buffer and cleaved overnight
626 with ULP-protease at 4°C. Cleaved DNAJB6 was diluted 5-fold before running through a cation exchange
627 column. SP Sepharose chromatography was conducted in 50 mM HEPES, pH 7.5 with a salt gradient from 5
628 M – 1 M NaCl. Fractions containing the protein were concentrated and subjected to size-exclusion on a
629 Superdex-75 16/600 column in 50 mM HEPES and 100 mM NaCl, pH 7.5. Through all stages of purification,
630 presence of DNAJB6 was monitored via SDS-PAGE.
631
632 DNAJB6 was labeled with Alexa Fluor™ 555 C_2 Maleimide (Thermo Scientific) following the manufacturer's
633 guidelines.
634
635 For LLPS experiments, concentrated, purified proteins (FUS, DNAJB6, and/or BSA) were diluted to 1.5 µM in
636 a 50 mM NaCl solution with 50mM Tris pH7.5 unless otherwise stated. For imaging, condensates were

637 maintained in PEG-silane coated Ibidi^{TM} coverslides to avoid wetting. Imaging was conducted with Zeiss
638 Axiovert 200M microscope with Improvision Openlab software using 100X magnification objective.
639
640 **TCSPC-FLIM**
641 mEmerald-tagged WT-FUS in NaCl solution (and DNAJB6) were mixed in milli-Q water, to give final protein
642 concentrations of 1 μM of WT-FUS, 0.16 μM WT-DNAJB6, and 60 mM NaCl. 7 μL of each condensate mixture
643 was deposited in individual silicon wells (Press-to-Seal, ThermoFisher Scientific) attached on 1.5 thickness
644 coverslips (Superior Marienfeld, Lauda-Konigshofen, Germany) for ageing and imaging. Samples were
645 imaged on a home-built confocal fluorescence microscope equipped with a time-correlated single photon
646 counting (TCSPC) module. A pulsed, supercontinuum laser (Fianium Whitelase, NKT Photonics,
647 Copenhagen, Denmark) provided excitation a repetition rate of 40 MHz. This was passed into a commercial
648 microscope frame (IX83, Olympus, Tokyo, Japan) through a 60x oil objective (PlanApo 60XOSC2, 1.4 NA,
649 Olympus). The excitation and emission beams are filtered through GFP-appropriate bandpass filters centered
650 at 474 and 542 (FF01-474/27-25, FF01-542/27, Semrock Inc., NY, USA). Laser scanning was performed using
651 a galvanometric mirror system (Quadscanner, Aberrior, Gottingen, Germany). Emission photons were
652 collected on a photon multiplier tube (PMT, PMC150, B&H GmBH, Berlin, Germany) and relayed to a time-
653 correlated single photon counting card (SPC830, B&H GmBH). Images were acquired at 256x256 pixels for
654 120 s (i.e., 10 cycles of 12 s). Photon counts were kept below 1% of laser emission photon (i.e., SYNC) rates
655 to prevent photon pile-up. TCSPC images were analysed using an in-house, MATLAB-based (MathWorks,
656 Natnick, MA, USA) phasor plot analysis script (https://github.com/LAG-MNG-
657 CambridgeUniversity/TCSPCPhasor), from which fluorescence lifetime maps and values were generated.
658 Fluorescence lifetimes are presented as those from individually segmented condensates from 9 images
659 (giving total a total of 86—209 condensates analysed per sample) taken over 3 fully independent experiments.
660 Statistical analysis was performed on Prism 6 (GraphPad, San Diego, CA, USA), where a one-way ANOVA
661 test with Holm-Sidak's multiple comparison was applied.
662
663 **Infrared Nanospectroscopy (AFM-IR)**
664 A nanoIR3 platform (Bruker) combining high resolution and low-noise AFM with a tunable quantum cascade
665 laser (QCL) with top illumination configuration was used. The sample morphology was scanned by the
666 nanoIR3 system, with a line rate within 0.1-0.4 Hz and in contact mode. A silicon gold coated probe with a
667 nominal radius of 30 nm and a cantilever with an elastic constant of about 0.2 N m^{-1} was used. Both infrared
668 (IR) spectra and maps were acquired by using phase loop (PLL) tracking of contact resonance, the phase was
669 zeroed to the desired off-resonant frequency on the left of the IR amplitude maximum and tracked with an
670 integral gain I=0.1-5 and proportional gain P=1-5. All images were acquired with a resolution above 500x100
671 pixels.
672

673 The AFM images were treated and analysed using SPIP software. The height images were first order flattened,
674 while IR and stiffness related maps were only flattened by a zero-order algorithm (offset). Nanoscale-localised
675 spectra were collected by placing the AFM tip on the top of the condensates with a laser wavelength sampling
676 of 2 cm^{-1} and a spectral speed of 100 cm^{-1}/s within the range 1462-1800 cm^{-1}. Within a single condensate, the
677 spectra were acquired at multiple nanoscale localised positions, the spectrum at each position being the co-
678 average of 5 spectra.
679
680 Successively, the spectra were treated by OriginPRO. They were smoothed by an adjacent averaging filter (5
681 pts) and a Savitzky-Golay filter (second order, 7 points) and normalised. Spectra second derivatives were
682 calculated, smoothed by a Savitzky-Golay filter (second order, 5 points). Relative secondary and quaternary
683 organisation was evaluated by integrating the area of the different secondary structural contributions in the
684 amide band I.
685
686 The spectra from 3 different condensates (FUS, n>100 ; FUS+DNAJB6, n>80) were averaged and used to
687 determine the secondary structure of the condensates. The error in the determination of the relative secondary
688 structure was calculated over the average of at least 5 independent spectra and it is < ±3%.
689
690 Spectra were analysed using the microscope's built-in Analysis Studio (Bruker) and OriginPRO (OriginLab).
691 All measurements were performed at room temperature, with laser power <2 mW and under controlled
692 Nitrogen atmosphere with residual real humidity below 5%.
693
694 **Mammalian Cell Lines and Cell Culture**
695 HEK293T cells used in this study were obtained from ATCC. Cells were maintained at 37°C in a humidified
696 atmosphere with 5% CO_2. HEK293T cells were grown in Dulbecco's Modified Eagle Medium (DMEM,
697 Invitrogen) which was supplemented with 10% fetal bovine serum (Gibco) and penicillin-streptomycin
698 (Invitrogen).
699
700 **Mammalian Transfection**
701 24 h prior to transfection, 293T cells were seeded at 40-60% confluency into 24-well plates coated for 30 min
702 with a 0.1 mg/mL solution of poly-D-lysine (MP Biomedicals Inc.) and washed with PBS (Gibco) once prior to
703 media and subsequent HEK293T cell addition. The next day, expression plasmid was incubated with Opti-
704 MEM (Gibco) and Lipofectamine 2000 (Invitrogen) for 30 min at room temperature prior to addition to cells,
705 per manufacturer protocol. 20 h after transfection, media was changed. Cells were harvested for protein
706 extraction and western blotting 48 h after transfection.
707
708 **Deep Mutational Scanning**

709 Deep mutational scanning libraries were prepared in biological duplicates, wherein PCR mutagenesis,
710 construction of bacterial libraries, and construction of yeast libraries were completed as independent
711 replicates. The DNAJB6 yeast expression vector, pAG413GAL-DNAJB6 was miniprepped immediately prior
712 to use. Variant versions of DNAJB6 were made by a single primer site-directed mutagenesis protocol. Oligos
713 were designed to introduce a degenerate codon, NNK, at each amino acid position. Additionally, each oligo
714 was designed to introduce 2-4 synonymous mutations at the codon immediately prior to the degenerate codon
715 to increase sampling diversity. For each codon, an individual mutagenesis single primer PCR reaction was
716 conducted in technical duplicates. The following PCR mix was used for mutagenesis: 5 µL 5X Q5 reaction
717 buffer, 0.5 µL 10 mM dNTPs, 150 ng DNA, 1.25 µL 10 µM primer, and H_2O to 25 µL. The following cycling
718 conditions were used: 1. 98°C, 45 s, 2. 98°C, 15 s, 3. 60°C, 15 s, 4. 72°C, 260 s, 5. Return to step 2 29X, 6.
719 72°C, 240 s. After PCR, the unmodified backbone was digested with 1 µL DpnI at 37°C for 1 h. After digestion,
720 independent PCR replicates were pooled and sets corresponding to 14 contiguous amino acids were pooled
721 together to enable data analysis using short read Illumina sequencing. 8 total sets were created encompassing
722 112 mutagenized amino acids. The combined sets were column purified with the Zymo DNA Clean &
723 Concentrator Kit. Each biological replicate of each set was transformed into electrocompetent 10-beta *E. Coli*
724 (New England Biolabs) in triplicate according to manufacturer instructions. Cells were plated following
725 outgrowth and recovery on 15 cm LB agar plates containing ampicillin and colonies were allowed to form for
726 24 h at 30°C. An individual typical transformation yielded 3-10 million colonies for a total of approximately 9-
727 30 million colonies for each biological replicate of each set. As a quality control measure, 20 colonies from
728 each set were sequenced to ensure editing. All colonies were scraped off plates and plasmid libraries were
729 purified by Midiprep (Zymo). Plasmid libraries were transformed into BY4741 containing the expression
730 plasmid pAG416GAL-FUS. Each biological replicate of each set was transformed in 96 separate
731 transformation reactions to ensure appropriate coverage and allowed 48 hours for outgrowth on SC -ura -his
732 plates at 30°C. Yeast libraries were scraped into 10 mL sterilized PBS and frozen in 20% glycerol. For
733 outgrowth, 600 µL of frozen yeast library was inoculated into 6 mL of SC -ura -his for 18 h in triplicate at 30°C
734 with rotation. After inoculation into galactose media, the remaining cells from the overnight cultures were spun
735 down at 4,000 rpm for 5 minutes and the pellets were frozen at -20°C. For each independent culture outgrowth,
736 12 µL of saturated overnight culture was inoculated into 6 mL of SC -ura -his galactose for 48 h at 30°C with
737 rotation. Each tube was centrifuged at 4,000 rpm for 5 minutes and the supernatant was discarded. Pellets
738 were resuspended in 300 µL of 200 mM LiOAc with 1% SDS and incubated for 15 minutes at 70°C with
739 shaking at 800 rpm. Afterwards, 900 µL 100% ethanol was added, tubes were vortexed, and centrifuged at
740 13,000 rpm for 10 minutes. Supernatant was discarded and pellets were allowed to air dry for 20 minutes
741 under flame. Pellets were then resuspended in 200 µL TE and incubated at 42°C for 20 minutes and then
742 centrifuged at 13,000 rpm for 10 minutes. The supernatant containing DNA was collected and stored for further
743 use. Each sample was then independently amplified and subsequently indexed for sequencing on a NextSeq
744 500/550 (Illumina). Depending on the set, amplification of the mutagenized region was done in 8 technical

745 replicates that were pooled after amplification. The following mix was used for all PCR reactions: 5 µL 5X Q5
746 reaction buffer, 0.5 µL 10 mM dNTPs, 0.5 µL DNA, 0.125 µL 100 µM forward primer, 0.125 µL 100 µM reverse
747 primer, 0.25 µL Q5 polymerase, and 18.5 µL H_2O. Amplification was done for 24 cycles for non-induced
748 libraries and 28 cycles for induced samples with the following conditions: 1. 98°C, 45 s, 2. 98°C, 15 s, 3. 58°C,
749 15 s, 4. 72°C, 30 s, 5. Return to step 2, either 24x or 28x 72°C, 240 s. After pooling, index sequences were
750 attached using the same PCR mix and cycling conditions, but for 8 cycles of amplification. Amplicons were
751 pooled according to set and amplicon length and gel purified to remove primers.
752 Sequencing data were processed on Illumina Basespace according to default QC settings and downloaded
753 as fastq files. Sequences were aligned using custom Python code. A raw activity score was calculated as:

754 $$\mathrm{Activity}_i = \log_2\left(\frac{\mathrm{Mut}_i}{\mathrm{WT}}\right)_{\mathrm{induced}} - \log_2\left(\frac{\mathrm{Mut}_i}{\mathrm{WT}}\right)_{\mathrm{uninduced}}$$

755 where the subscript i denotes individual unique variants. Mut_i denotes the average number of counts of the
756 particular mutant codon of interest, averaged over all codings, while WT denotes the number of counts of
757 the wild-type nucleotide sequence. Raw activity scores were then normalized across sets by anchoring stop
758 codon mutants to -1 and WT to 0 to eliminate set by set variation that may have arisen due to experimental
759 fluctuation. The final normalized activity scores are presented in heatmap format for easy visualization.
760 Plotted "wild-type" values are derived from the recoded versions of the wild-type residue at a given position
761 and thus do not always have a 0 value. Raw sequencing reads have been uploaded to the NCBI SRA under
762 BioProject PRJNA769721 (SUB10503160).
763
764 **Cas9 Knockout of DNAJB6**
765 A Cas9 expressing HEK293T cell line was generated in a well of a 24-well dish by transfecting 300 ng of pB-
766 CAGGS-Cas9-SV40-BPSV40 vector a long with 100 ng of a plasmid expressing the Piggybac transposase
767 (System Biosciences, LLC) with Lipofectamine 2000 according to manufacturer protocols (Invitrogen). Media
768 was changed 24 h after transfection before selecting with Noursethricin N-Acetyl Transferase (NAT) at 300
769 µg/mL 48 h after transfection. Cells were expanded and continuously selected with NAT for 2 weeks before
770 being frozen down for further use.
771
772 A gRNA lentivirus compatible plasmid encoding two guide RNAs from the Brunello library
773 (GCATATGAAGTGCTGTCGGA and GACTTCTTTGGGAATCGAAG) targeting DNAJB6 was created.
774 Lentivirus was created from this plasmid by co-transfecting HEK293T cells with this plasmid alongside
775 psPAX2 (Addgene #12260) and MD2.G (Addgene #12259). After transfection and a media change 24 h
776 after transfection, media containing lentivirus was harvested 72 h later. Lentivirus containing media was
777 added to Cas9 containing cells for 24 h before a media change. Beginning 48 h after the media change,
778 cells were exposed to 2 weeks of alternating drug selections of NAT at 500 µg/mL and Blasticidin at 2 µg/mL
779 every 48 h with regular splitting, to ensure both Cas9 and gRNA maintained good expression and were not

780 silenced during the outgrowth process. After 2 weeks, single cells were sorted into 96 well plates using the
781 Bigfoot Spectral Cell Sorter (Thermo). To gate on single cells, forward scatter and side scatter were used to
782 isolate single cells and sort them into 100 µL of media. Single cells were allowed to expand for 2 weeks
783 under alternating drug selection. DNA was harvested with QuickExtract (Lucigen) according to manufacturer
784 protocols. PCR primers spanning individual cut sites in addition to primers spanning a potential deletion
785 were used to amplify out the region of DNAJB6 subject to cutting. PCR products were sanger sequenced
786 and TIDE was used to analyze sanger fragments to confirm disruption of DNAJB6[77]. To confirm loss of
787 DNAJB6, western blots were performed. The same process was repeated with non-targeting control guide
788 RNAs (AAAAAGCTTCCGCCTGATGG and AAAACAGGACGATGTGCGGC).
789
790 **RNA-seq**
791 HEK293T cells were transfected as previously described with 50 ng of expression plasmid and grown for 72
792 hours in a 24 well dish after transfection. Cells were harvested in TRIzol and stored at -80°C. RNA was
793 harvested from cells with the Direct-zol miniprep kit (Zymo). Harvested RNA was prepared for sequencing
794 with the NEBNext® Ultra™ II RNA Library Prep Kit for Illumina (NEB). Two biological replicates were
795 performed for each condition. Each individual replicate was amplified with a unique combination of indexing
796 primers after the adaptor ligation step to uniquely identify it. Pooled libraries were combined and sequenced
797 with a 75 cycles NextSeq 500/550 High Output Kit on a NextSeq 550 machine (Illumina). Each replicate was
798 allocated ~30 million reads. Reads were aligned to the hg19 genome using HISAT2 to obtain counts.
799 Differential expression was calculated using limma. Raw sequencing reads have been uploaded to the NCBI
800 SRA under BioProject PRJNA769721 (SUB10426285).
801
802 **Human ORFeome Library construction**
803 The pooled hORFeome V8.1 library was inserted into the pAG413GAL-ccdb-6Stop vector with Gateway LR
804 II Clonase Enzyme mix (Invitrogen) at a ratio of 150ng:50ng. The reaction was incubated overnight at 25°C.
805 Expression plasmids were electroporated into electrocompetent 10-beta *E. Coli* (NEB) and ~200,000
806 colonies were harvested and Miniprepped. The expression plasmid library was transformed into BY4742 and
807 selected in SC -his glucose plates for 48 hours. Individual colonies were picked and arrayed into 96 well
808 plates and saved. To identify the ORF present in each well, each plate was process individually. A total of 20
809 pools per plate were made, consisting of 12 column pools and 8 row pools. DNA from each of these pools
810 was then obtained using a LiOAc-based extraction. ORFs within each pool were amplified for 30 cycles with
811 general primers binding to the galactose promoter and cyc terminator and subsequently column purified. 250
812 ng of the purified PCR product was processed with the NEBNext Ultra II FS DNA Library Prep Kit for
813 Illumina (NEB) according to manufacturer protocols. After adaptor ligation and prior to indexing, a forward
814 primer placed 60 bp upstream from the ATG start codon was used in combination with an adaptor reverse
815 primer and amplified for 13 cycles to selectively enrich for the human ORF containing fragment in

816 preparation for sequencing. Each individual pool was then uniquely indexed and sequenced with a 150
817 cycles NextSeq 500/550 High Output Kit on a NextSeq 500/550 machine (Illumina). After sequencing, the
818 identity of each well was determined by its presence in a specific combination of row and column wells.

References

1 Hebert, L. E., Weuve, J., Scherr, P. A. & Evans, D. A. Alzheimer disease in the United States (2010-2050) estimated using the 2010 census. *Neurology* **80**, 1778-1783, doi:10.1212/WNL.0b013e31828726f5 (2013).

2 Vanni, S., Colini Baldeschi, A., Zattoni, M. & Legname, G. Brain aging: A Ianus-faced player between health and neurodegeneration. *J Neurosci Res* **98**, 299-311, doi:10.1002/jnr.24379 (2020).

3 Cavazzoni, P. *The Path Forward: Advancing Treatments and Cures for Neurodegenerative Diseases*, <https://www.fda.gov/news-events/congressional-testimony/path-forward-advancing-treatments-and-cures-neurodegenerative-diseases-07292021> (2021).

4 Labbadia, J. & Morimoto, R. I. The biology of proteostasis in aging and disease. *Annu Rev Biochem* **84**, 435-464, doi:10.1146/annurev-biochem-060614-033955 (2015).

5 Hipp, M. S., Kasturi, P. & Hartl, F. U. The proteostasis network and its decline in ageing. *Nat Rev Mol Cell Biol* **20**, 421-435, doi:10.1038/s41580-019-0101-y (2019).

6 Outeiro, T. F. & Lindquist, S. Yeast cells provide insight into alpha-synuclein biology and pathobiology. *Science* **302**, 1772-1775, doi:10.1126/science.1090439 (2003).

7 Armakola, M. *et al.* Inhibition of RNA lariat debranching enzyme suppresses TDP-43 toxicity in ALS disease models. *Nat Genet* **44**, 1302-1309, doi:10.1038/ng.2434 (2012).

8 Sun, Z. *et al.* Molecular determinants and genetic modifiers of aggregation and toxicity for the ALS disease protein FUS/TLS. *PLoS Biol* **9**, e1000614, doi:10.1371/journal.pbio.1000614 (2011).

9 Gitler, A. D. Beer and bread to brains and beyond: can yeast cells teach us about neurodegenerative disease? *Neurosignals* **16**, 52-62, doi:10.1159/000109759 (2008).

10 Kim, H. J. *et al.* Therapeutic modulation of eIF2α phosphorylation rescues TDP-43 toxicity in amyotrophic lateral sclerosis disease models. *Nat Genet* **46**, 152-160, doi:10.1038/ng.2853 (2014).

11 Cooper, A. A. *et al.* Alpha-synuclein blocks ER-Golgi traffic and Rab1 rescues neuron loss in Parkinson's models. *Science* **313**, 324-328, doi:10.1126/science.1129462 (2006).

12 Couthouis, J. *et al.* A yeast functional screen predicts new candidate ALS disease genes. *Proc Natl Acad Sci U S A* **108**, 20881-20890, doi:10.1073/pnas.1109434108 (2011).

13 Kryndushkin, D., Ihrke, G., Piermartiri, T. C. & Shewmaker, F. A yeast model of optineurin proteinopathy reveals a unique aggregation pattern associated with cellular toxicity. *Mol Microbiol* **86**, 1531-1547, doi:10.1111/mmi.12075 (2012).

14 Treusch, S. *et al.* Functional links between Aβ toxicity, endocytic trafficking, and Alzheimer's disease risk factors in yeast. *Science* **334**, 1241-1245, doi:10.1126/science.1213210 (2011).

15 Ju, S. *et al.* A yeast model of FUS/TLS-dependent cytotoxicity. *PLoS Biol* **9**, e1001052, doi:10.1371/journal.pbio.1001052 (2011).

16 Chen, Y. C. *et al.* Randomized CRISPR-Cas Transcriptional Perturbation Screening Reveals Protective Genes against Alpha-Synuclein Toxicity. *Mol Cell* **68**, 247-257.e245, doi:10.1016/j.molcel.2017.09.014 (2017).

17 Lee, J. C. *et al.* Inhibition of p38 MAP kinase as a therapeutic strategy. *Immunopharmacology* **47**, 185-201, doi:10.1016/s0162-3109(00)00206-x (2000).

18 Jo, M. *et al.* Yeast genetic interaction screen of human genes associated with amyotrophic lateral sclerosis: identification of MAP2K5 kinase as a potential drug target. *Genome Res* **27**, 1487-1500, doi:10.1101/gr.211649.116 (2017).

19 Guerrero, E. N. *et al.* TDP-43/FUS in motor neuron disease: Complexity and challenges. *Prog Neurobiol* **145-146**, 78-97, doi:10.1016/j.pneurobio.2016.09.004 (2016).

20 Yan, Z. *et al.* Yeast Barcoders: a chemogenomic application of a universal donor-strain collection carrying bar-code identifiers. *Nat Methods* **5**, 719-725, doi:10.1038/nmeth.1231 (2008).

21 Schmierer, B. *et al.* CRISPR/Cas9 screening using unique molecular identifiers. *Mol Syst Biol* **13**, 945, doi:10.15252/msb.20177834 (2017).

22 Kim, H. J. *et al.* Mutations in prion-like domains in hnRNPA2B1 and hnRNPA1 cause multisystem proteinopathy and ALS. *Nature* **495**, 467-473, doi:10.1038/nature11922 (2013).

23 Suzuki, H. & Matsuoka, M. The Lysosomal Trafficking Transmembrane Protein 106B Is Linked to Cell Death. *J Biol Chem* **291**, 21448-21460, doi:10.1074/jbc.M116.737171 (2016).

24 Jovičić, A. *et al.* Modifiers of C9orf72 dipeptide repeat toxicity connect nucleocytoplasmic transport defects to FTD/ALS. *Nat Neurosci* **18**, 1226-1229, doi:10.1038/nn.4085 (2015).
25 Zheng, C., Geetha, T. & Babu, J. R. Failure of ubiquitin proteasome system: risk for neurodegenerative diseases. *Neurodegener Dis* **14**, 161-175, doi:10.1159/000367694 (2014).
26 Arndt, V., Rogon, C. & Höhfeld, J. To be, or not to be--molecular chaperones in protein degradation. *Cell Mol Life Sci* **64**, 2525-2541, doi:10.1007/s00018-007-7188-6 (2007).
27 Jackrel, M. E. *et al.* Potentiated Hsp104 variants antagonize diverse proteotoxic misfolding events. *Cell* **156**, 170-182, doi:10.1016/j.cell.2013.11.047 (2014).
28 Ioakeimidis, F. *et al.* A splicing mutation in the novel mitochondrial protein DNAJC11 causes motor neuron pathology associated with cristae disorganization, and lymphoid abnormalities in mice. *PLoS One* **9**, e104237, doi:10.1371/journal.pone.0104237 (2014).
29 Chen, X. & Petranovic, D. Amyloid-β peptide-induced cytotoxicity and mitochondrial dysfunction in yeast. *FEMS Yeast Res* **15**, doi:10.1093/femsyr/fov061 (2015).
30 Keefer, K. M., Stein, K. C. & True, H. L. Heterologous prion-forming proteins interact to cross-seed aggregation in Saccharomyces cerevisiae. *Scientific Reports* **7**, 5853, doi:10.1038/s41598-017-05829-5 (2017).
31 Higurashi, T., Hines, J. K., Sahi, C., Aron, R. & Craig, E. A. Specificity of the J-protein Sis1 in the propagation of 3 yeast prions. *Proceedings of the National Academy of Sciences* **105**, 16596-16601, doi:10.1073/pnas.0808934105 (2008).
32 Breslow, D. K. *et al.* A comprehensive strategy enabling high-resolution functional analysis of the yeast genome. *Nat Methods* **5**, 711-718, doi:10.1038/nmeth.1234 (2008).
33 Park, S. K. *et al.* Development and validation of a yeast high-throughput screen for inhibitors of $A\beta_{42}$ oligomerization. *Dis Model Mech* **4**, 822-831, doi:10.1242/dmm.007963 (2011).
34 Sarnoski, E. A., Liu, P. & Acar, M. A High-Throughput Screen for Yeast Replicative Lifespan Identifies Lifespan-Extending Compounds. *Cell Rep* **21**, 2639-2646, doi:10.1016/j.celrep.2017.11.002 (2017).
35 Wong, L. H. *et al.* A yeast chemical genetic screen identifies inhibitors of human telomerase. *Chem Biol* **20**, 333-340, doi:10.1016/j.chembiol.2012.12.008 (2013).
36 Zhang, L. *et al.* A high-throughput screen for chemical inhibitors of exocytic transport in yeast. *Chembiochem* **11**, 1291-1301, doi:10.1002/cbic.200900681 (2010).
37 Kachroo, A. H. *et al.* Evolution. Systematic humanization of yeast genes reveals conserved functions and genetic modularity. *Science* **348**, 921-925, doi:10.1126/science.aaa0769 (2015).
38 Uhlén, M. *et al.* Proteomics. Tissue-based map of the human proteome. *Science* **347**, 1260419, doi:10.1126/science.1260419 (2015).
39 Thiruvalluvan, A. *et al.* DNAJB6, a Key Factor in Neuronal Sensitivity to Amyloidogenesis. *Mol Cell* **78**, 346-358.e349, doi:10.1016/j.molcel.2020.02.022 (2020).
40 Brehme, M. *et al.* A chaperome subnetwork safeguards proteostasis in aging and neurodegenerative disease. *Cell Rep* **9**, 1135-1150, doi:10.1016/j.celrep.2014.09.042 (2014).
41 Fan, C. Y., Lee, S. & Cyr, D. M. Mechanisms for regulation of Hsp70 function by Hsp40. *Cell Stress Chaperones* **8**, 309-316, doi:10.1379/1466-1268(2003)008<0309:mfrohf>2.0.co;2 (2003).
42 Kampinga, H. H. & Craig, E. A. The HSP70 chaperone machinery: J proteins as drivers of functional specificity. *Nat Rev Mol Cell Biol* **11**, 579-592, doi:10.1038/nrm2941 (2010).
43 Gillis, J. *et al.* The DNAJB6 and DNAJB8 protein chaperones prevent intracellular aggregation of polyglutamine peptides. *J Biol Chem* **288**, 17225-17237, doi:10.1074/jbc.M112.421685 (2013).
44 Kakkar, V. *et al.* The S/T-Rich Motif in the DNAJB6 Chaperone Delays Polyglutamine Aggregation and the Onset of Disease in a Mouse Model. *Mol Cell* **62**, 272-283, doi:10.1016/j.molcel.2016.03.017 (2016).
45 Månsson, C. *et al.* DNAJB6 is a peptide-binding chaperone which can suppress amyloid fibrillation of polyglutamine peptides at substoichiometric molar ratios. *Cell Stress Chaperones* **19**, 227-239, doi:10.1007/s12192-013-0448-5 (2014).
46 Hageman, J. *et al.* A DNAJB chaperone subfamily with HDAC-dependent activities suppresses toxic protein aggregation. *Mol Cell* **37**, 355-369, doi:10.1016/j.molcel.2010.01.001 (2010).

47 Harms, M. B. *et al.* Exome sequencing reveals DNAJB6 mutations in dominantly-inherited myopathy. *Ann Neurol* **71**, 407-416, doi:10.1002/ana.22683 (2012).
48 Bengoechea, R., Pittman, S. K., Tuck, E. P., True, H. L. & Weihl, C. C. Myofibrillar disruption and RNA-binding protein aggregation in a mouse model of limb-girdle muscular dystrophy 1D. *Hum Mol Genet* **24**, 6588-6602, doi:10.1093/hmg/ddv363 (2015).
49 Chen, H. J. *et al.* The heat shock response plays an important role in TDP-43 clearance: evidence for dysfunction in amyotrophic lateral sclerosis. *Brain* **139**, 1417-1432, doi:10.1093/brain/aww028 (2016).
50 Udan-Johns, M. *et al.* Prion-like nuclear aggregation of TDP-43 during heat shock is regulated by HSP40/70 chaperones. *Hum Mol Genet* **23**, 157-170, doi:10.1093/hmg/ddt408 (2014).
51 Murakami, T. *et al.* ALS/FTD Mutation-Induced Phase Transition of FUS Liquid Droplets and Reversible Hydrogels into Irreversible Hydrogels Impairs RNP Granule Function. *Neuron* **88**, 678-690, doi:10.1016/j.neuron.2015.10.030 (2015).
52 Khong, A. *et al.* The Stress Granule Transcriptome Reveals Principles of mRNA Accumulation in Stress Granules. *Mol Cell* **68**, 808-820.e805, doi:10.1016/j.molcel.2017.10.015 (2017).
53 Markmiller, S. *et al.* Context-Dependent and Disease-Specific Diversity in Protein Interactions within Stress Granules. *Cell* **172**, 590-604 e513, doi:10.1016/j.cell.2017.12.032 (2018).
54 Patel, A. *et al.* A Liquid-to-Solid Phase Transition of the ALS Protein FUS Accelerated by Disease Mutation. *Cell* **162**, 1066-1077, doi:10.1016/j.cell.2015.07.047 (2015).
55 Qamar, S. *et al.* FUS Phase Separation Is Modulated by a Molecular Chaperone and Methylation of Arginine Cation-π Interactions. *Cell* **173**, 720-734.e715, doi:10.1016/j.cell.2018.03.056 (2018).
56 Krainer, G. *et al.* Reentrant liquid condensate phase of proteins is stabilized by hydrophobic and non-ionic interactions. *Nat Commun* **12**, 1085, doi:10.1038/s41467-021-21181-9 (2021).
57 Itzhak, D. N., Tyanova, S., Cox, J. & Borner, G. H. Global, quantitative and dynamic mapping of protein subcellular localization. *Elife* **5**, doi:10.7554/eLife.16950 (2016).
58 Kato, M. *et al.* Cell-free formation of RNA granules: low complexity sequence domains form dynamic fibers within hydrogels. *Cell* **149**, 753-767, doi:10.1016/j.cell.2012.04.017 (2012).
59 Ruggeri, F. S. *et al.* Infrared nanospectroscopy characterization of oligomeric and fibrillar aggregates during amyloid formation. *Nat Commun* **6**, 7831, doi:10.1038/ncomms8831 (2015).
60 Ruggeri, F. S. *et al.* Influence of the β-sheet content on the mechanical properties of aggregates during amyloid fibrillization. *Angew Chem Int Ed Engl* **54**, 2462-2466, doi:10.1002/anie.201409050 (2015).
61 Shimanovich, U. *et al.* Silk micrococoons for protein stabilisation and molecular encapsulation. *Nat Commun* **8**, 15902, doi:10.1038/ncomms15902 (2017).
62 Ruggeri, F. S., Mannini, B., Schmid, R., Vendruscolo, M. & Knowles, T. P. J. Single molecule secondary structure determination of proteins through infrared absorption nanospectroscopy. *Nat Commun* **11**, 2945, doi:10.1038/s41467-020-16728-1 (2020).
63 Ruggeri, F. S. *et al.* The Influence of Pathogenic Mutations in α-Synuclein on Biophysical and Structural Characteristics of Amyloid Fibrils. *ACS Nano* **14**, 5213-5222, doi:10.1021/acsnano.9b09676 (2020).
64 Harmon, T. S., Holehouse, A. S., Rosen, M. K. & Pappu, R. V. Intrinsically disordered linkers determine the interplay between phase separation and gelation in multivalent proteins. *Elife* **6**, doi:10.7554/eLife.30294 (2017).
65 Gu, J. *et al.* Hsp40 proteins phase separate to chaperone the assembly and maintenance of membraneless organelles. *Proc Natl Acad Sci U S A* **117**, 31123-31133, doi:10.1073/pnas.2002437117 (2020).
66 Weston, S. *et al.* A Yeast Suppressor Screen Used To Identify Mammalian SIRT1 as a Proviral Factor for Middle East Respiratory Syndrome Coronavirus Replication. *J Virol* **93**, doi:10.1128/jvi.00197-19 (2019).
67 Fernández-Acero, T. *et al.* A yeast-based in vivo bioassay to screen for class I phosphatidylinositol 3-kinase specific inhibitors. *J Biomol Screen* **17**, 1018-1029, doi:10.1177/1087057112450051 (2012).

975 68 Conicella, A. E., Zerze, G. H., Mittal, J. & Fawzi, N. L. ALS Mutations Disrupt Phase Separation
976 Mediated by α-Helical Structure in the TDP-43 Low-Complexity C-Terminal Domain. *Structure* **24**,
977 1537-1549, doi:10.1016/j.str.2016.07.007 (2016).
978 69 Tosatto, L. *et al.* Single-molecule FRET studies on alpha-synuclein oligomerization of Parkinson's
979 disease genetically related mutants. *Sci Rep* **5**, 16696, doi:10.1038/srep16696 (2015).
980 70 López-Erauskin, J. *et al.* ALS/FTD-Linked Mutation in FUS Suppresses Intra-axonal Protein
981 Synthesis and Drives Disease Without Nuclear Loss-of-Function of FUS. *Neuron* **100**, 816-
982 830.e817, doi:10.1016/j.neuron.2018.09.044 (2018).
983 71 Thelen, M. P. & Kye, M. J. The Role of RNA Binding Proteins for Local mRNA Translation:
984 Implications in Neurological Disorders. *Front Mol Biosci* **6**, 161, doi:10.3389/fmolb.2019.00161
985 (2019).
986 72 Birsa, N. *et al.* FUS-ALS mutants alter FMRP phase separation equilibrium and impair protein
987 translation. *Sci Adv* **7**, doi:10.1126/sciadv.abf8660 (2021).
988 73 Yu, H. *et al.* HSP70 chaperones RNA-free TDP-43 into anisotropic intranuclear liquid spherical
989 shells. *Science* **371**, doi:10.1126/science.abb4309 (2021).
990 74 Aprile, F. A. *et al.* The molecular chaperones DNAJB6 and Hsp70 cooperate to suppress α-synuclein
991 aggregation. *Sci Rep* **7**, 9039, doi:10.1038/s41598-017-08324-z (2017).
992 75 Månsson, C. *et al.* Interaction of the molecular chaperone DNAJB6 with growing amyloid-beta 42
993 (Aβ42) aggregates leads to sub-stoichiometric inhibition of amyloid formation. *J Biol Chem* **289**,
994 31066-31076, doi:10.1074/jbc.M114.595124 (2014).
995 76 Li, W. *et al.* MAGeCK enables robust identification of essential genes from genome-scale
996 CRISPR/Cas9 knockout screens. *Genome Biol* **15**, 554, doi:10.1186/s13059-014-0554-4 (2014).
997 77 Brinkman, E. K., Chen, T., Amendola, M. & van Steensel, B. Easy quantitative assessment of
998 genome editing by sequence trace decomposition. *Nucleic Acids Res* **42**, e168,
999 doi:10.1093/nar/gku936 (2014).
1000 78 Sondheimer, N., Lopez, N., Craig, E. A. & Lindquist, S. The role of Sis1 in the maintenance of the
1001 [RNQ+] prion. *Embo j* **20**, 2435-2442, doi:10.1093/emboj/20.10.2435 (2001).
1002 79 Bagriantsev, S. N., Gracheva, E. O., Richmond, J. E. & Liebman, S. W. Variant-specific [PSI+]
1003 infection is transmitted by Sup35 polymers within [PSI+] aggregates with heterogeneous protein
1004 composition. *Mol Biol Cell* **19**, 2433-2443, doi:10.1091/mbc.e08-01-0078 (2008).
1005 80 Barlow, J. T., Bogatyrev, S. R. & Ismagilov, R. F. A quantitative sequencing framework for absolute
1006 abundance measurements of mucosal and lumenal microbial communities. *Nat Commun* **11**, 2590,
1007 doi:10.1038/s41467-020-16224-6 (2020).
1008 81 McIntyre, L. M. *et al.* RNA-seq: technical variability and sampling. *BMC Genomics* **12**, 293,
1009 doi:10.1186/1471-2164-12-293 (2011).
1010

1011 **Acknowledgements**

1012 We thank members of the Chavez lab for helpful discussions and insights regarding the project. Aaron Gitler
1013 provided initial insight and a number of yeast disease models, for which we are immensely grateful. We
1014 thank the ALS Stem Cell Core Program at Columbia University Irving Medical Center and its members,
1015 Hynek Wichterle, Jon Costa, Emily Lowry, and Niraj Ramsamooj for helpful discussions regarding cell-based
1016 assays and for valuable reagents. Vlad Korobeynikov provided helpful guidance and insight into western
1017 blotting and protein extraction from cells. Matt Harms provided helpful discussion regarding DNAJB6 patient
1018 mutations and insight into interpretation of DMS results. Edwin Chan provided the SoxN plasmids. Richard
1019 Gardner provided the PAB1 poly-alanine plasmids. Priya Banerjee provided insight into the phase
1020 separation properties of DNAJB6 and FUS. Divyansh Argawal provided helpful discussions regarding
1021 statistical analysis of the screening platform. Debbie Hong and Sho Iketani provided valuable guidance on

how to perform our deep mutational scanning studies. A.C. is supported by a Career Awards for Medical Scientists from the Burroughs Wellcome Fund and a Therapeutic Idea Award (#AL190073) from the DoD, and a fellowship award to the laboratory from Project ALS. S.J.R is supported by NIH grant F31NS111851. J.W. is supported by NSF grant 2113646. N.Z. is supported by NIH grant 2R01HG006137-10.

Author contributions

A.C. conceived the project. A.C., S.J.R., S.Q., N.S., and P.S.G. planned and designed experiments. S.J.R. and A.C. performed yeast multiplexed screening. S.J.R. and L.H.H. performed secondary validation testing. S.J.R. and J.S. performed and conducted analysis on deep mutational scanning approaches. S.J.R. and S.M. made cell lines. S.J.R. performed mammalian cell culture assays. S.Q. and J.N. performed *in vitro* studies with DNAJB6 and FUS. C.W.C, C.F.K, and G.S.K.S. performed FLIM experiments. X.C and F.S.R performed AFM-IR experiments. S.J.R., N.Z., and J.W. designed and performed analysis. S.J.R. and A.C. wrote the manuscript with input from all authors.

Competing interests

A.C. and S.J.R. are inventors on a patent application submitted on the screening technology described in this work.

Data and materials availability

All reagents generated in this study will be deposited to Addgene. Code used for analysis of the screening approach is available at the Chavez group github account (https://github.com/ChavezResearchLab).

Figures

Figure 1. Screening of molecular chaperones from yeast and humans for their ability to rescue the proteotoxicity of various neurodegenerative disease and protein misfolding models. **a.** Models included in screen and disease association. **b.** Log2 fold change plotted for interactions between selected yeast chaperones and models. Log2 fold changes are shown as an average of all barcoded strains associated with that model **c.** Statistically significant interactions between selected yeast chaperones and models. **d.** Validation of interactions between yeast chaperones and models. Data are shown as mean ± s.d. for three biological replicates. **e.** Log2 fold change plotted for interactions between selected human chaperones and models **f.** Statistically significant interactions between selected human chaperones and models. **g.** Validation of interactions between human chaperones and models. Data are shown as mean ± s.d. for three biological replicates. Comparisons between two conditions were conducted with Welch's t tests while multiple comparisons were conducted with ordinary one-way ANOVA; **P≤0.01, ***P≤0.001, ****P≤0.0001.

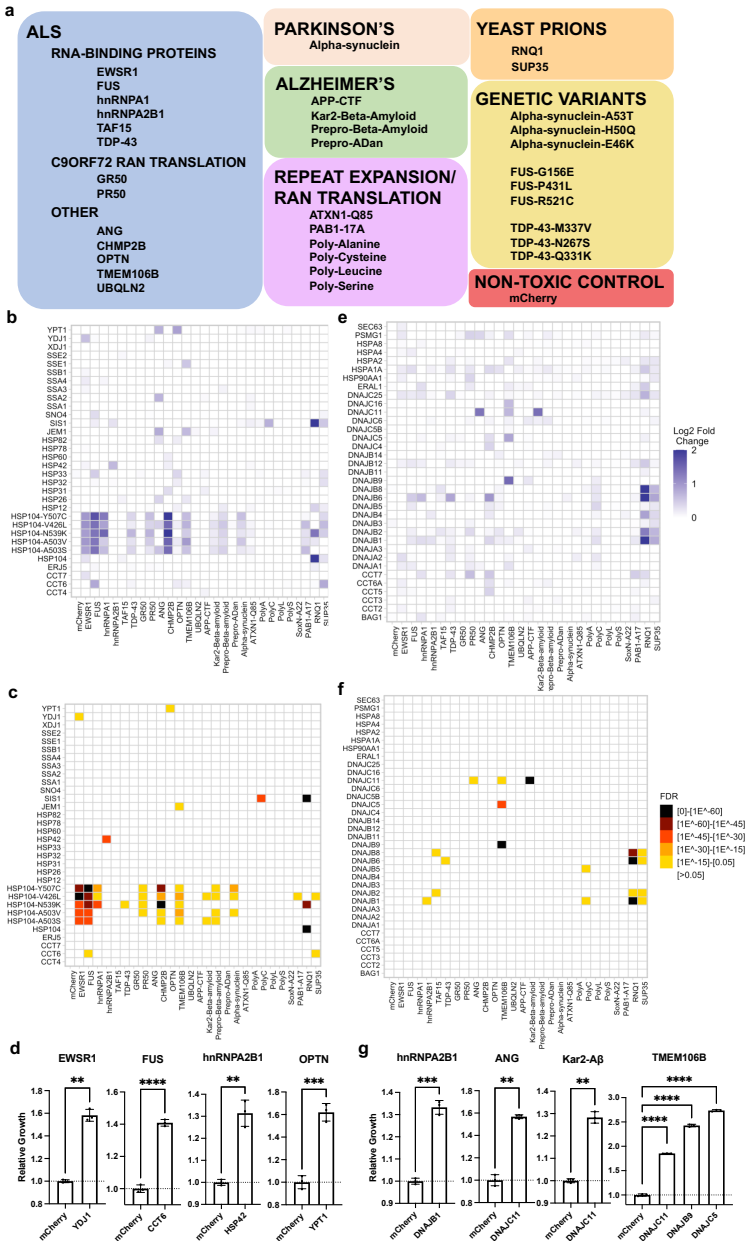

Figure 2. DNAJB6 is a rescuer of FUS, TDP-43, and hnRNPA1. a. DNAJB6 rescues proteotoxicity of FUS, TDP-43, and hnRNPA1 in yeast. Data are shown as mean ± s.d. for three biological replicates. **b-d.** Overexpression of FUS, TDP-43, and hnRNPA1 in HEK293T cells results in formation of SDS-insoluble (RIPA buffer insoluble), urea-soluble species**.** The formation of these species can be reduced by co-expression of DNAJB6. **e.** Quantification of the urea soluble species normalized to total protein detected by Ponceau S staining in b-d. Each independent replicate was normalized to its associated EYFP rescued sample. **f.** Validation of non-target control (NTC) and DNAJB6 KO lines. DNAJB6 has two isoforms; DNAJB6a and DNAJB6b, which are 36 kDa and 27 kDa in size, respectively. **g-i.** Overexpression of FUS, TDP-43, and hnRNPA1 in DNAJB6 KO lines shows an increase in the propensity to form SDS-insoluble, urea-soluble species. **j.** Quantification of the urea soluble species normalized to total protein detected by Ponceau S staining in g-j. Each independent replicate was normalized its associated EYFP rescued sample. All data are shown as mean ± s.d. for three biological replicates. All statistical tests were conducted with Welch's t tests; ns = not significant P>0.05, *P≤0.05, **P≤0.01, ***P≤0.001, ****P≤0.0001.

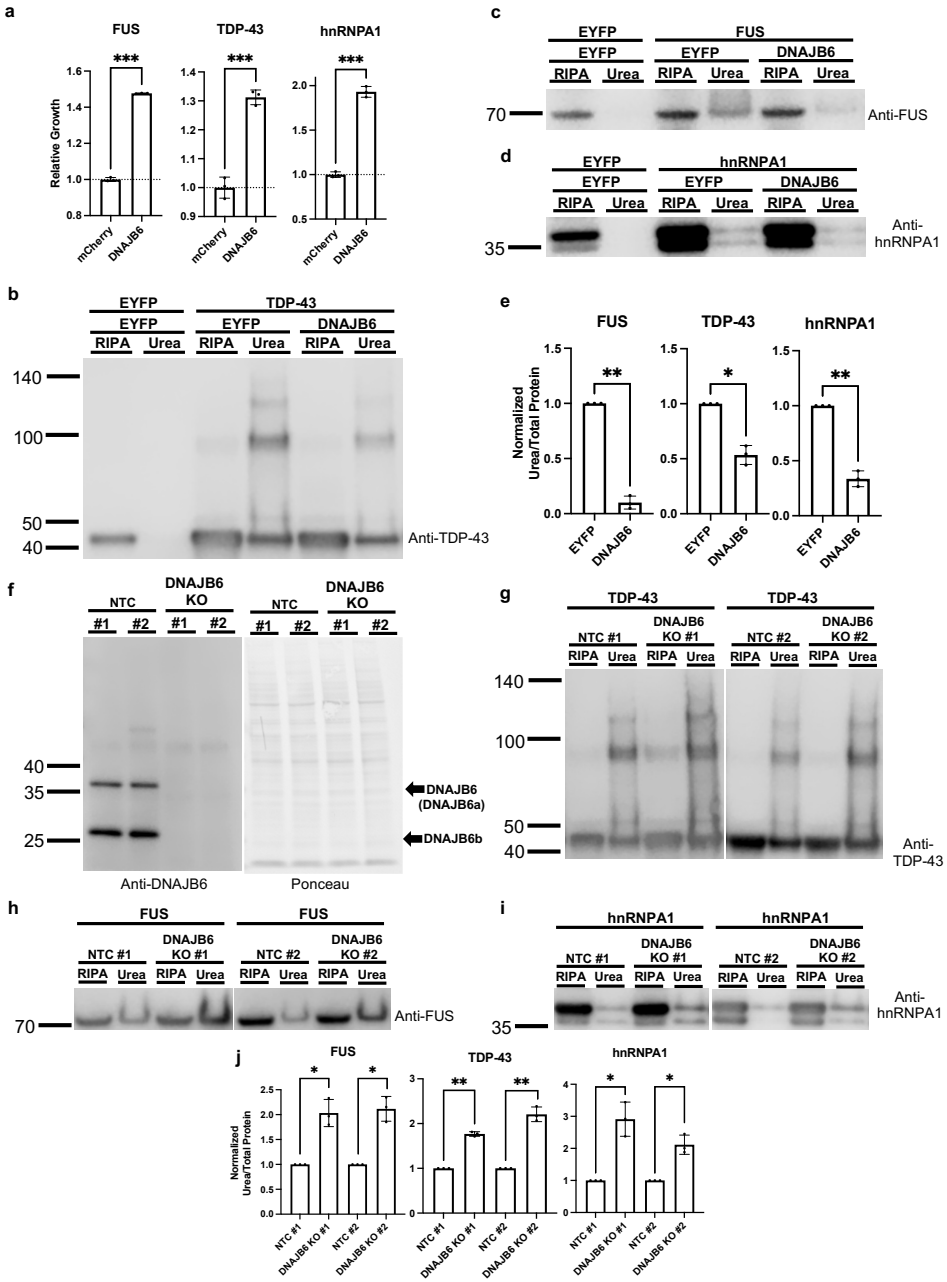

Figure 3. DNAJB6 modulates the dynamics and structure of FUS condensates. a. FUS and FUS + DNAJB6 condensates at 20 minutes and 24 hours. Scale bar = 10 µm. **b.** Quantification of condensate size as shown in panel a. 1 micron squared minimum size cutoff was used when quantifying condensates. Average condensate size was determined for multiple condensates within several different fields of view. At 20 minutes n=343 for FUS and n=1,455 for FUS + DNAJB6. At 24 hours, n=792 for FUS and n=1,459 for FUS + DNAJB6. Comparisons were conducted with Welch's two-sided t test. ****P≤0.0001 Plots are shown as mean +/- SEM. **c.** FUS condensates form fibrillar aggregates when incubated for 36 hours. FUS condensates do not form fibrillar aggregates in the presence of DNAJB6 at 36 hours. Scale bar = 20 µm. **d.** Condensate-averaged fluorescence lifetimes. Results are based on 86 - 326 condensates from 9 images taken over 3 independent experiments. One-way ANOVA (Holm-Sidak's multiple comparison test), where **** is P<0.0001. **e.** IR average spectra from 3 independent FUS or FUS + DNAJB6 condensates and second derivative of the amide I band to deconvolve protein secondary structure contributions. **f.** Quantification of secondary structure within condensates by AFM-IR.

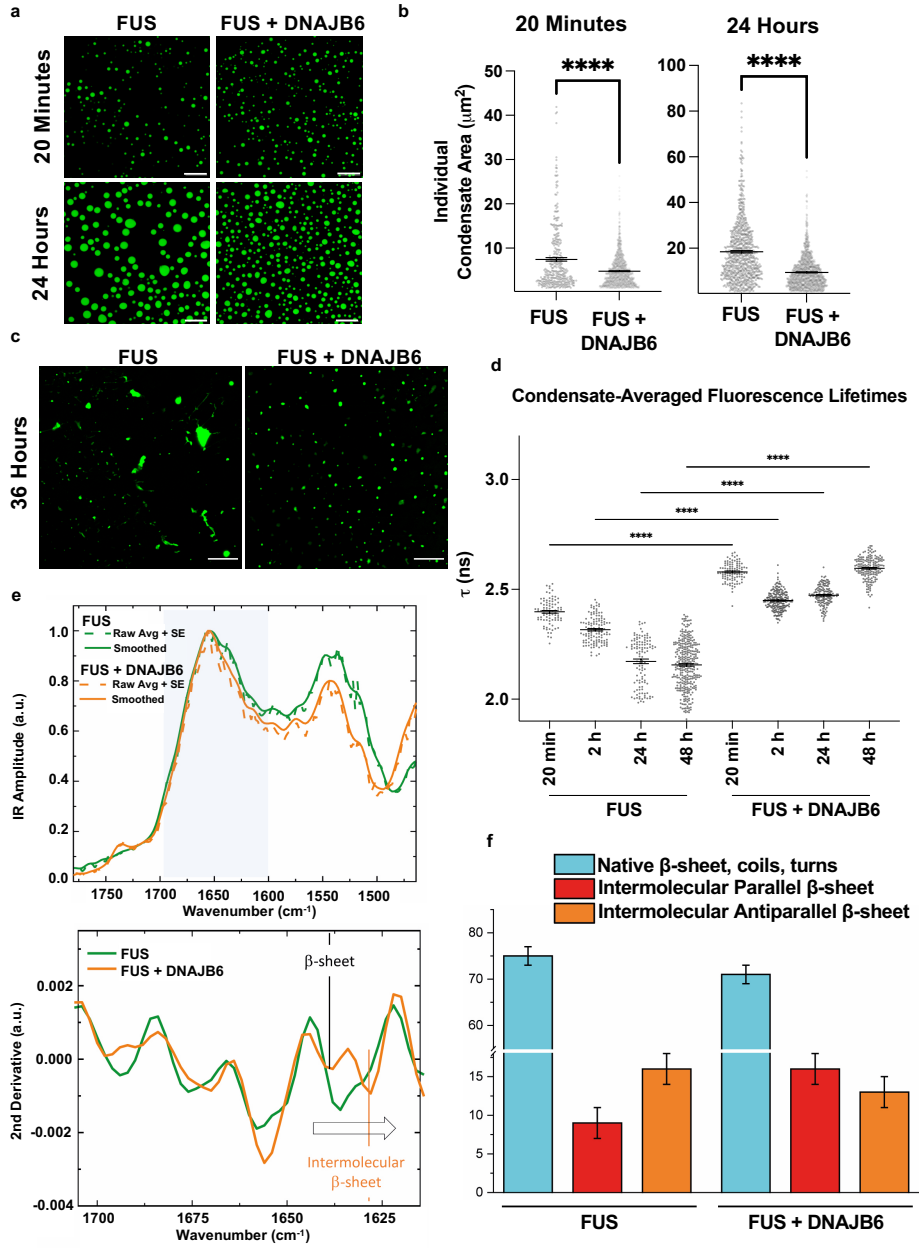

Figure 4. Deep Mutational Scan (DMS) of DNAJB6 identifies potentiated variants. **a.** Overview of DMS approach for testing DNAJB6 variants against the FUS model. A library of DNAJB6 mutants is generated using a site directed mutagenesis-based approach, the resulting plasmid library is transformed into yeast containing the FUS model and grown under inducing conditions, finally the relative growth rates of all mutants are determined and normalized to the wild-type DNAJB6 variant. **b**. DMS heatmap for residues 83-194 of DNAJB6. Intensity of blue or red colored boxes indicates increased or decreased activity as compared to the wild-type DNAJB6 protein. * indicates stop codon mutation, black dots (•) mark the wild-type residue for each site in the protein. **c.** Validation of DMS results in the FUS model and testing of variants against the TDP-43 model. **d.** Testing of potentiated DNAJB6 variants in mammalian cells for their ability to reduce SDS-insoluble, urea-soluble FUS species upon overexpression. **e.** Quantification of the urea soluble species normalized to total protein detected by Ponceau S staining in d. Each independent replicate was normalized its associated EYFP rescued sample. All data are shown as mean ± s.d. for three biological replicates. Comparisons were conducted with ordinary one-way ANOVA with display of significant comparisons; *P≤0.05, **P≤0.01, ***P≤0.001, ****P≤0.0001.

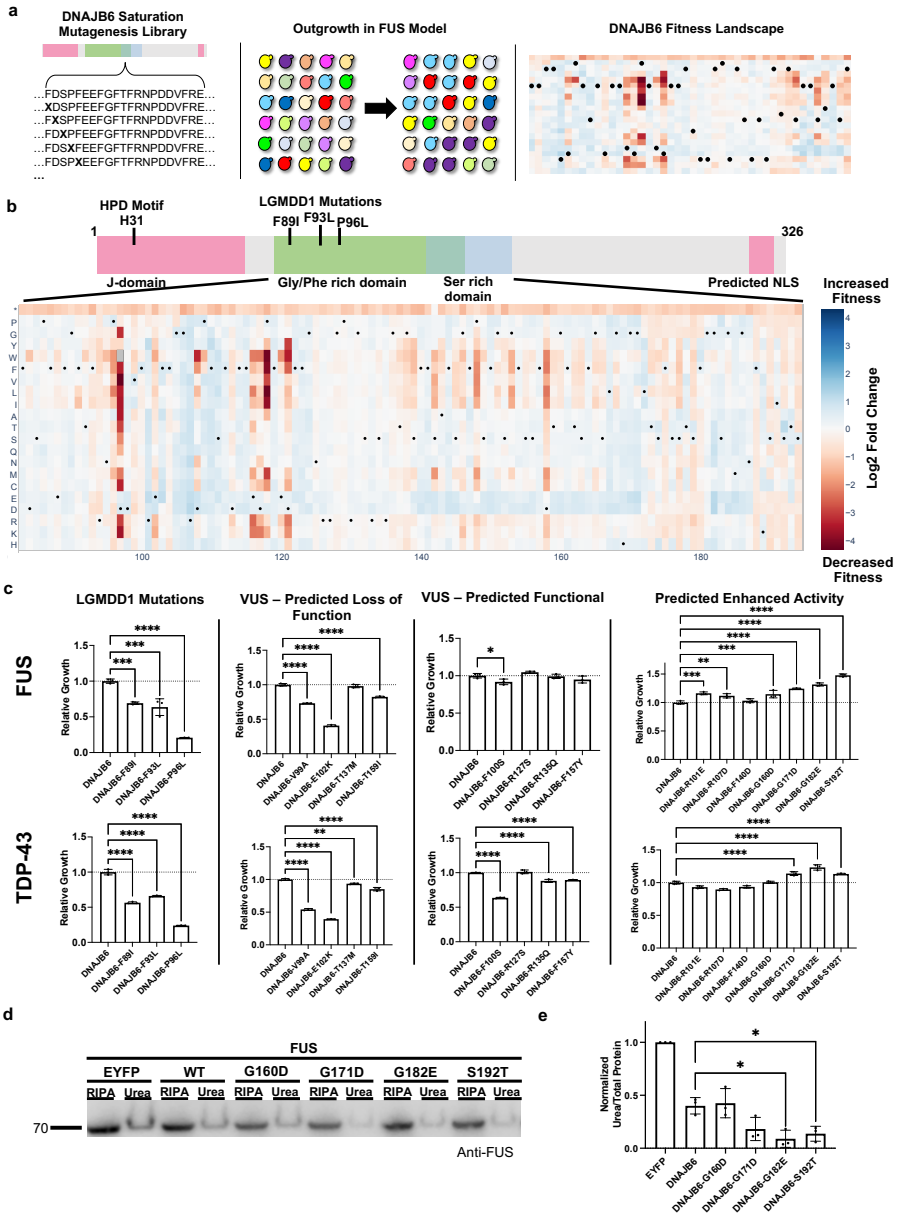

1100 **Supplementary Figures**

1101 **Supplementary Figure 1. Detailed development of a multiplexed screening platform. a.** Individual
1102 yeast strains containing an integrated DNA barcode are transformed with a construct encoding an
1103 aggregation-prone protein associated with neurodegeneration before pooling. **b.** Rescuers are introduced *en*
1104 *masse* through mating and selection. **c.** Mated barcode pools are grown in inducing media in 96-well plate
1105 format before DNA harvesting, NGS, and subsequent analysis.

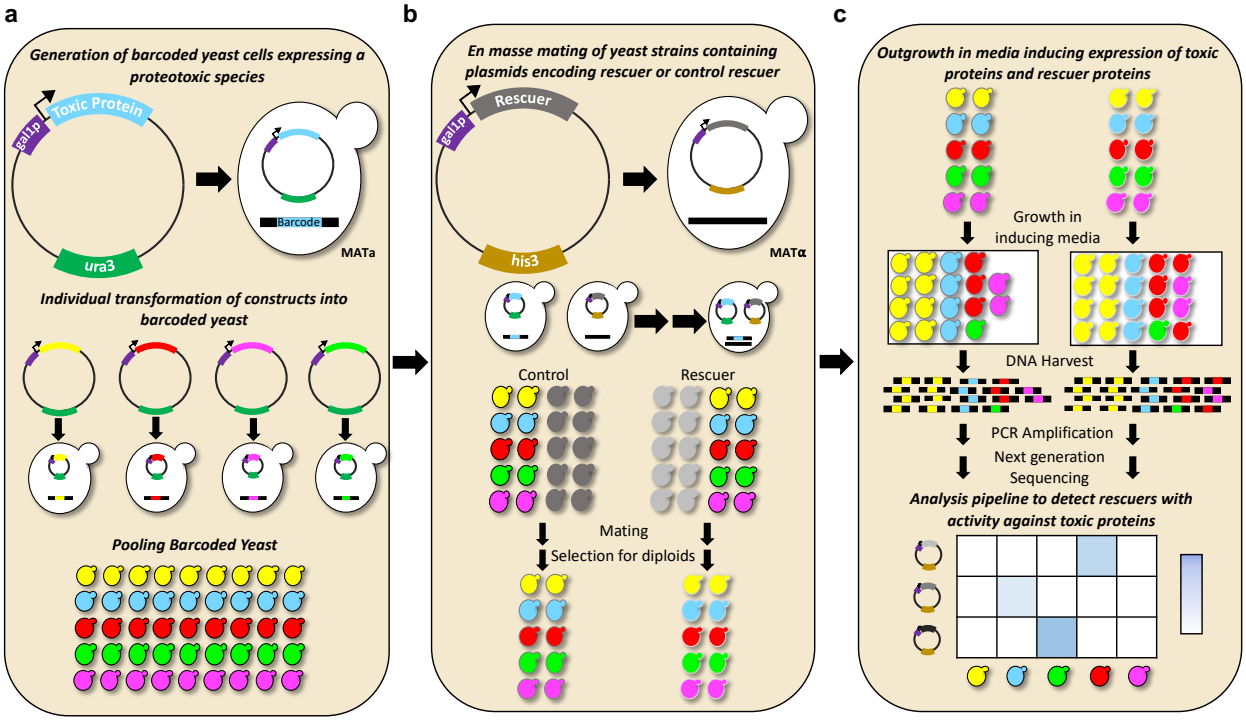

1106

Supplementary Figure 2. *En masse* mating of a barcode pool and outgrowth of a mated barcoded pool do not perturb barcode ratios. a. Example of correlation plot between two separately mated pools that have been selected for diploids, each dot represents a different barcode within the population. **b.** Correlation values for 36 comparisons between the barcode abundance for separately mated pools. **c.** Example of correlation plot between two separately mated pools that have been selected for diploids, and outgrown in inducing media, each dot represents a different barcode within the population. **d.** Correlation values for 36 comparisons between separately mated and outgrown pools.

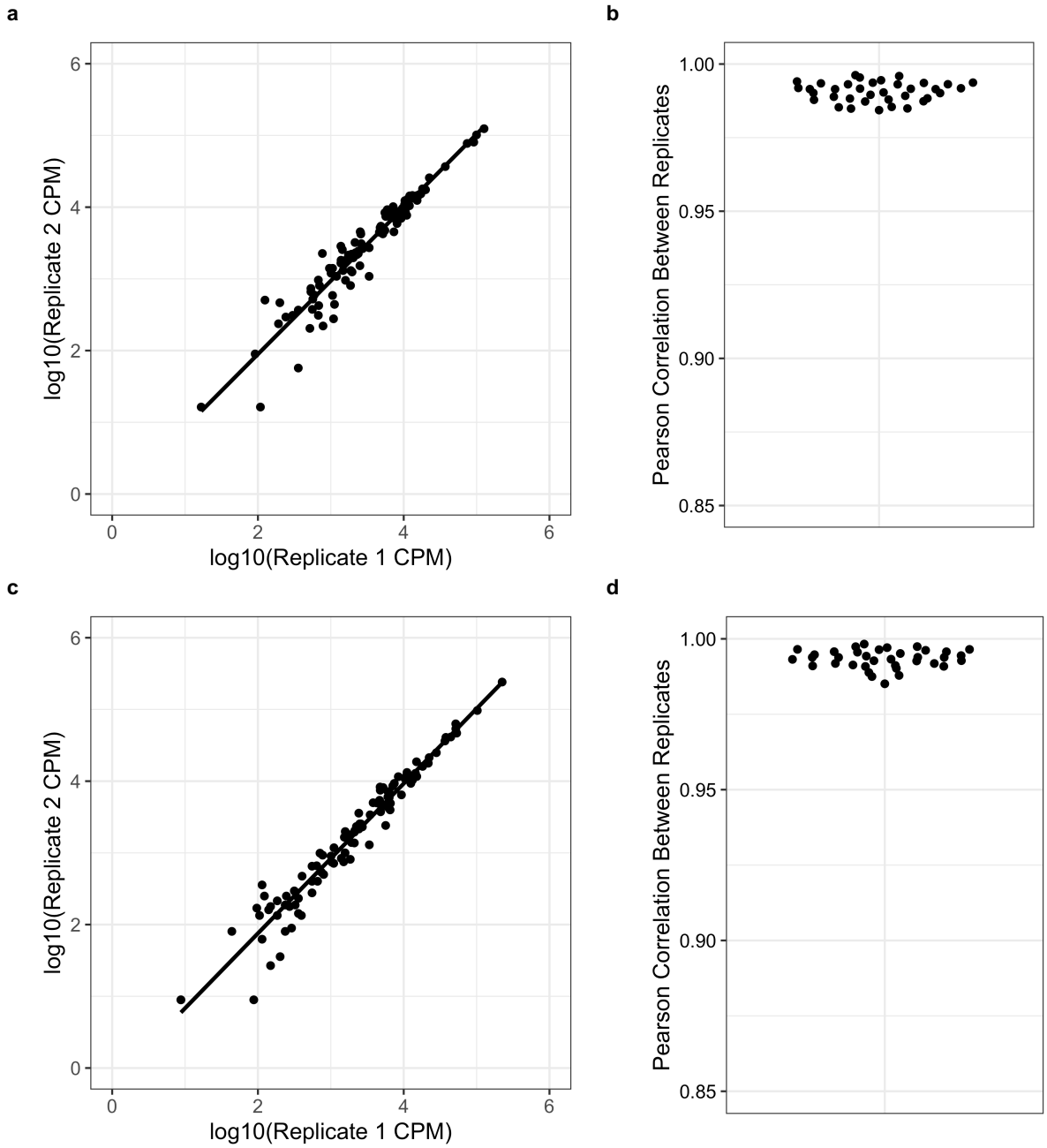

1115 **Supplementary Figure 3. Comparison of three pooling strategies for detecting known interactions**. **a.**
1116 Log2 fold change heatmaps for 3 pooling strategies. Previously known interactions that are expected are
1117 outlined in purple **b.** Correlations between barcodes after pooled barcoded strains were mated to the same
1118 control rescuer, selected for diploids, and grown under inducing condition using each of the three different
1119 pooling strategies. **c.** Coefficient of variation vs. relative barcode abundance plot for each of the 3 pooling
1120 strategies.

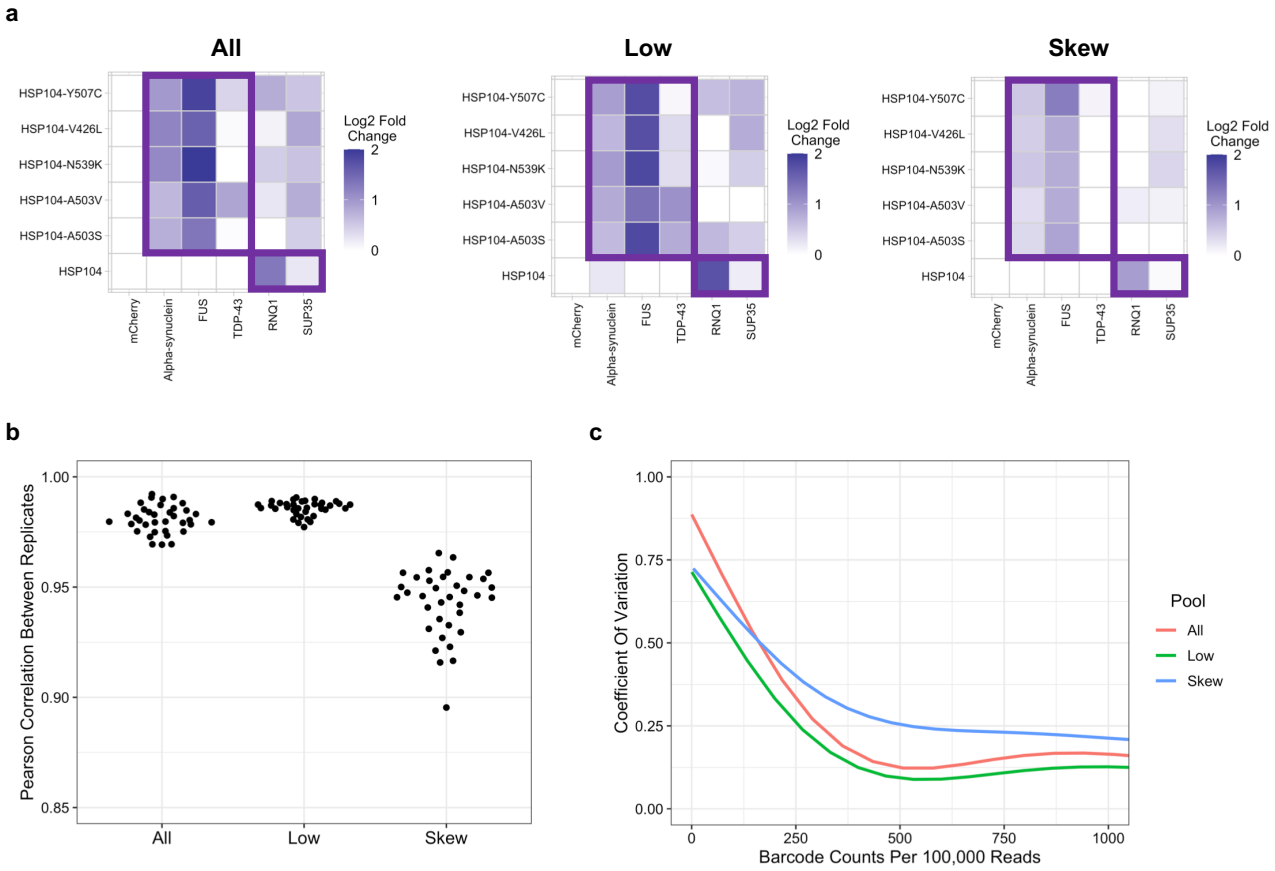

1121

1122 **Supplementary Figure 4. Exploration of biological and technical sources of error for the optimal**
1123 **screening strategy. a.** Correlation between biological replicates (separately mated, selected, outgrown,
1124 harvested, and PCR amplified) and technical replicates (same sample of harvested DNA separately PCR
1125 amplified). **b.** Coefficient of variation vs. relative barcode abundance plot for biological replicates of pooled
1126 DNA-barcoded library mated to an inert rescuer demonstrating the effect of averaging between biological
1127 replicates. **c.** Coefficient of variation vs. relative barcode abundance plot for technical replicates of pooled
1128 DNA-barcoded library mated to an inert rescuer demonstrating effect of averaging between technical
1129 replicates.

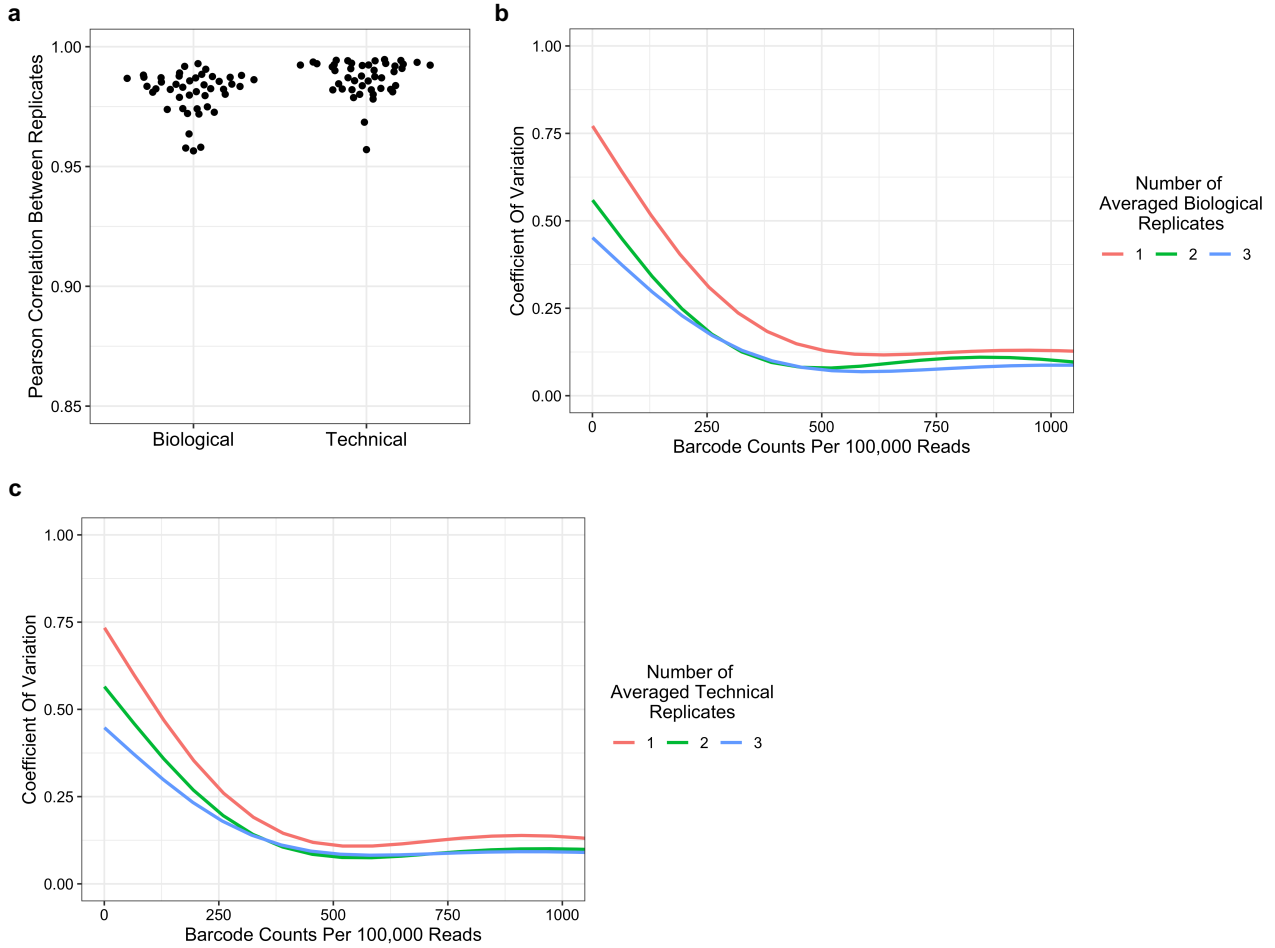

1130

1131 **Supplementary Figure 5. Validation of the optimized multiplexed screening approach using known**
1132 **genetic interactions. a.** Optimized conditions enable detection of positive control interactions in pilot screen
1133 **b-g.** Spot assay validation of tested interactions in pilot multiplexed screen.

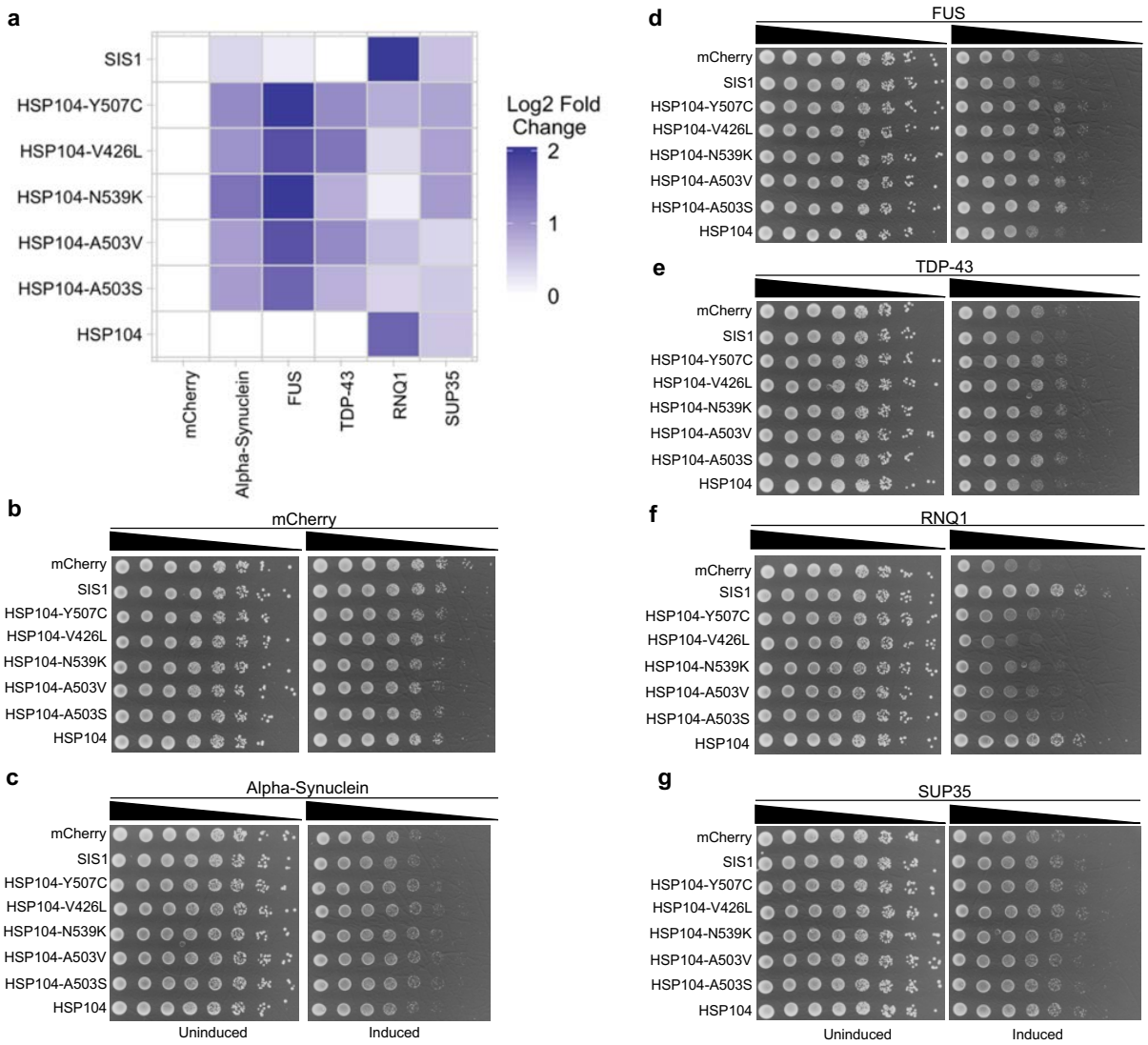

1134

1135 **Supplementary Figure 6. Simulation of how redundant barcoding enhances the ability to reject the**
1136 **null hypothesis.** Fold change required for rejection of null hypothesis simulated using optimized pooling
1137 conditions with two biological replicates and two technical replicates.

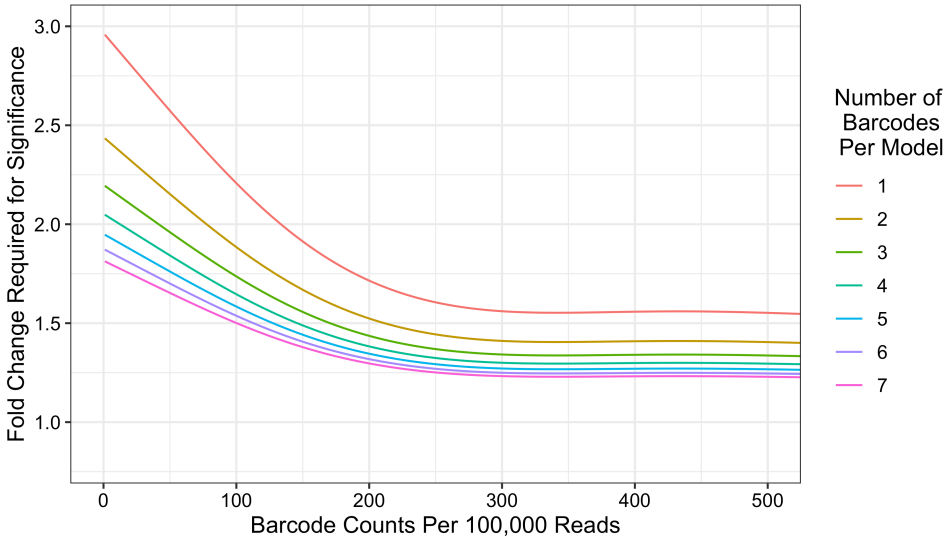

1138
1139

1140 **Supplementary Figure 7. Determination of number of reads required to adequately sample 302-**
1141 **member DNA-barcoded pool**. **a.** Coefficient of variation vs. relative barcode abundance for DNA-barcoded
1142 library mated to an inert rescuer at different levels of read subsampling. **b.** Number of individual barcoded
1143 strains with less than 10 raw reads at different levels of read subsampling.

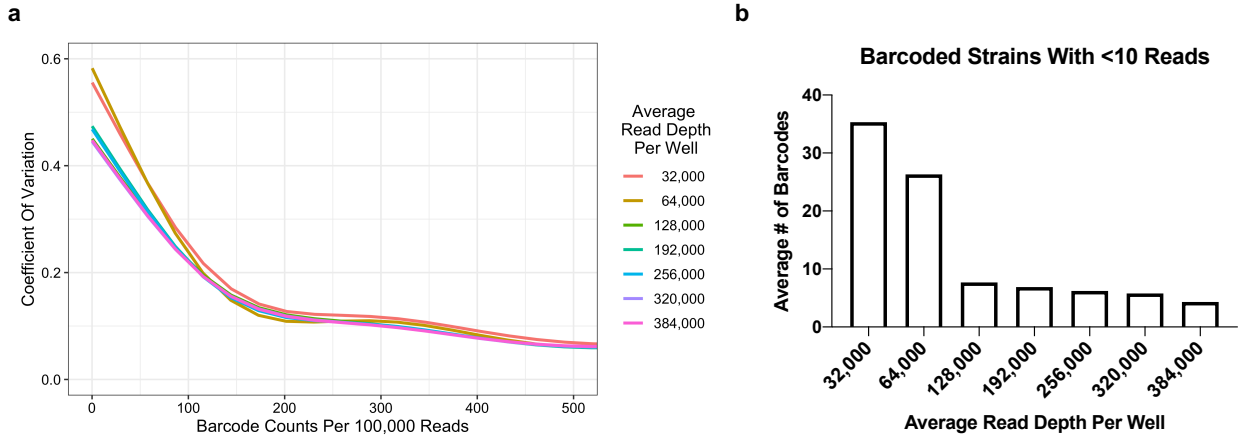

1144

Supplementary Figure 8. Full yeast chaperone screen. a. Log2 fold change interactions between all tested yeast chaperones and the models included in the pool. **b.** Significant interactions between yeast chaperones and models included in the pool.

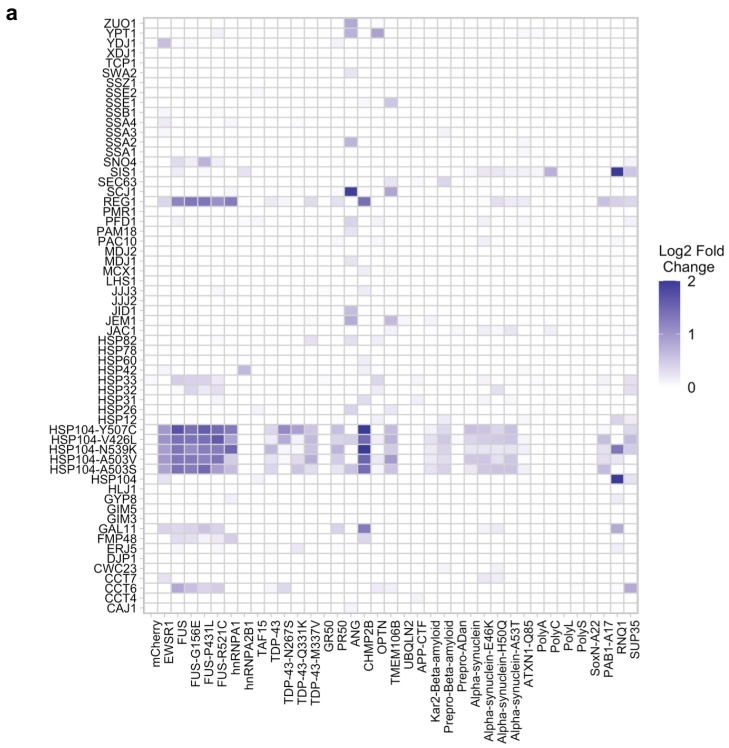

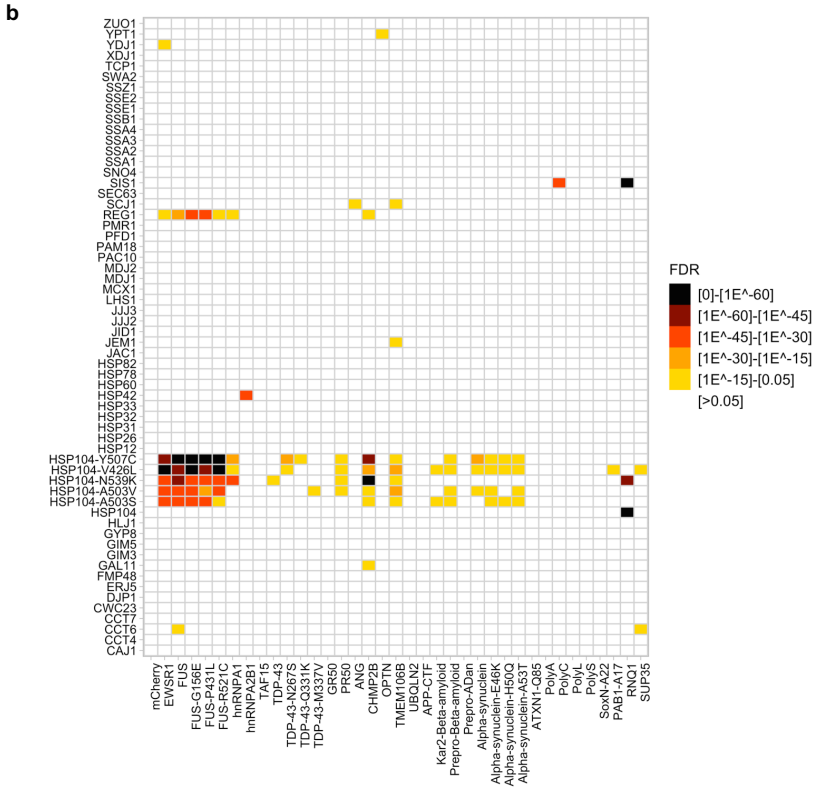

Supplementary Figure 9. Full human chaperone screen. a. Log2 fold change interactions between all tested human chaperones and the models included in the pool. **b.** Significant interactions between human chaperones and models included in the pool.

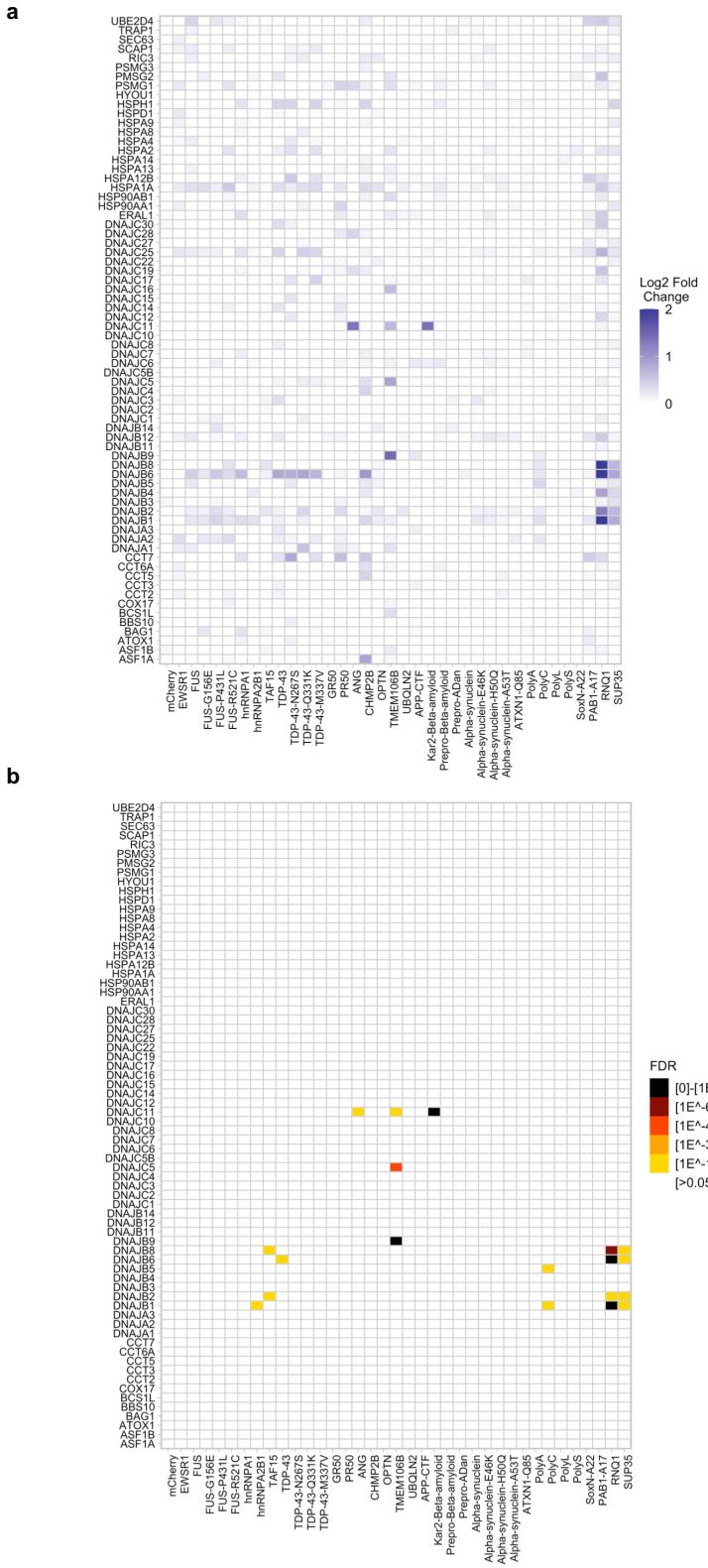

1153 **Supplementary Figure 10. Validation of liquid culture growth assay.** The interactions tested in our pilot
1154 screen for **a.** mCherry **b.** Alpha-synuclein **c.** FUS **d.** TDP-43 **e.** RNQ1 and **f.** SUP-35 and validated with spot
1155 assays were re-tested with the liquid culture growth assay to validate its behavior. Data are shown as mean
1156 ± s.d. for three biological replicates. Comparisons were conducted with ordinary one-way ANOVA with
1157 display of comparisons of interactions with in positive changes in relative growth; ns = not significant,
1158 *P≤0.05, **P≤0.01, ***P≤0.001, ****P≤0.0001.

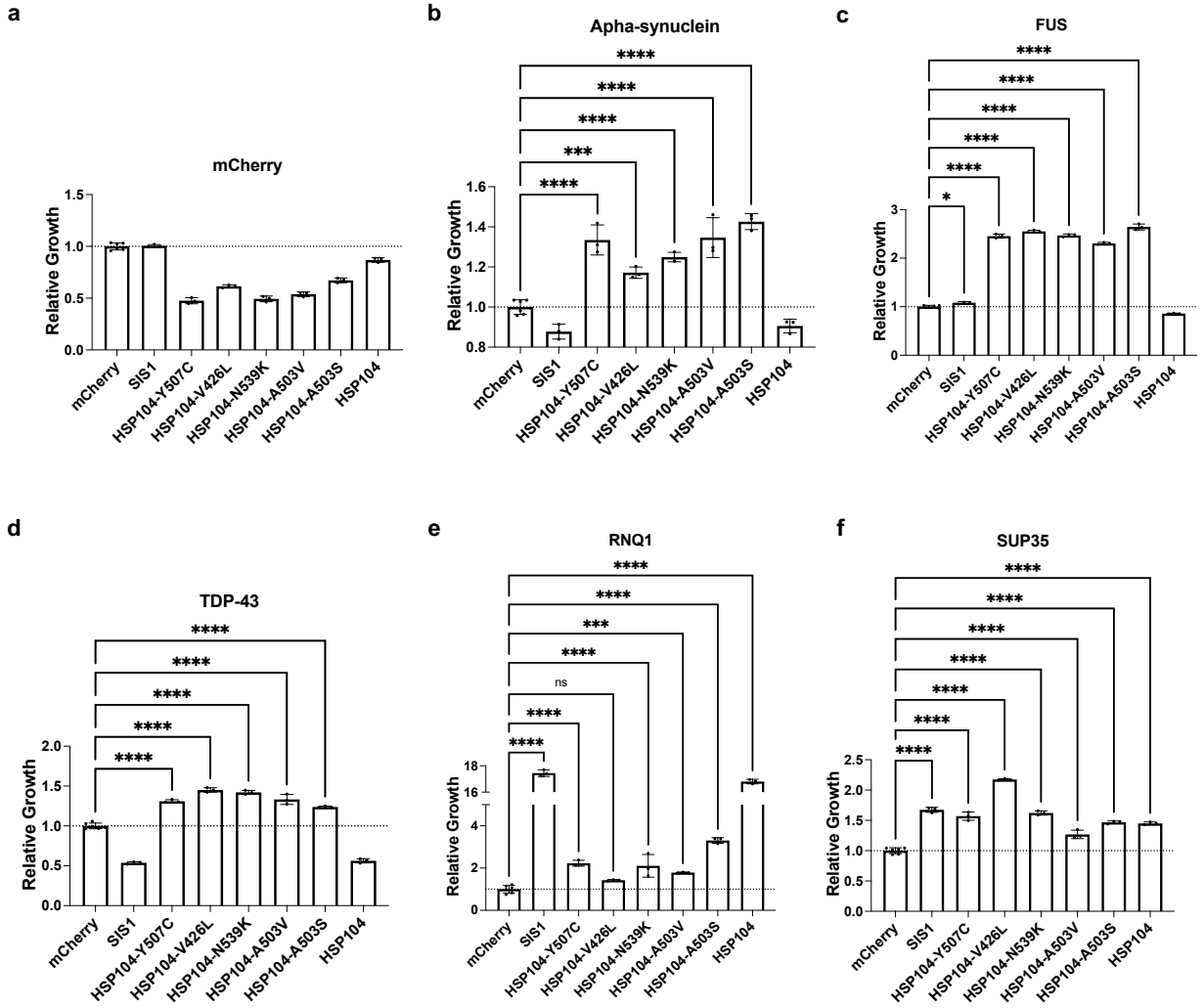

1159

Supplementary Figure 11. Subsampling of barcodes per model demonstrates power of redundant barcoding. Yeast and human rescuers with called hits were reanalyzed with fewer number of barcoded strains included in the analysis. All hits shown in the 5-7 Barcodes/Model condition were validated.

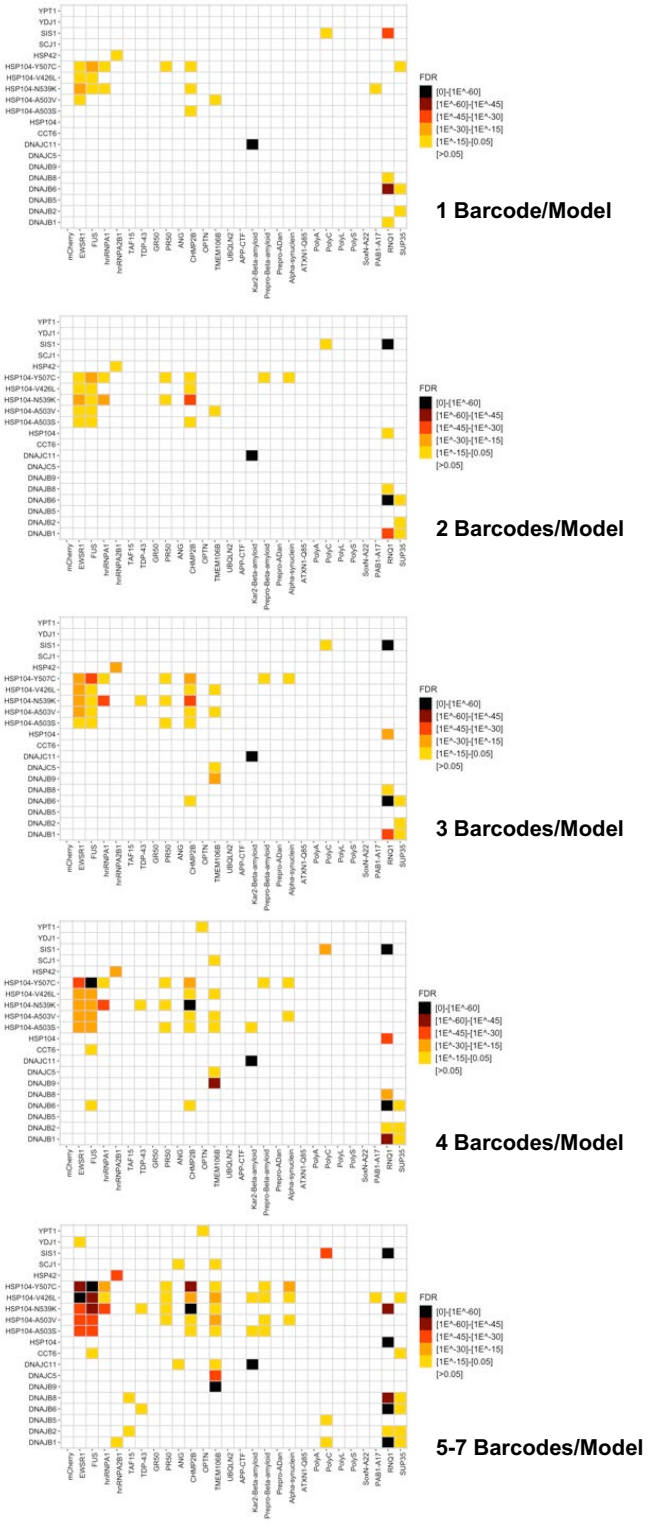

Supplementary Figure 12. DNAJB6 shows specific activity against FUS, TDP-43, and hnRNPA1. a-c. DNAJB6 was tested alongside other human HSP40 proteins for their ability to rescue **a.** FUS, **b.** TDP-43, and **c.** hnRNPA1 proteotoxicity in yeast. Comparisons were conducted with ordinary one-way ANOVA with display of comparisons of interactions with in positive changes in relative growth; *P≤0.05, ***P≤0.001, ****P≤0.0001.

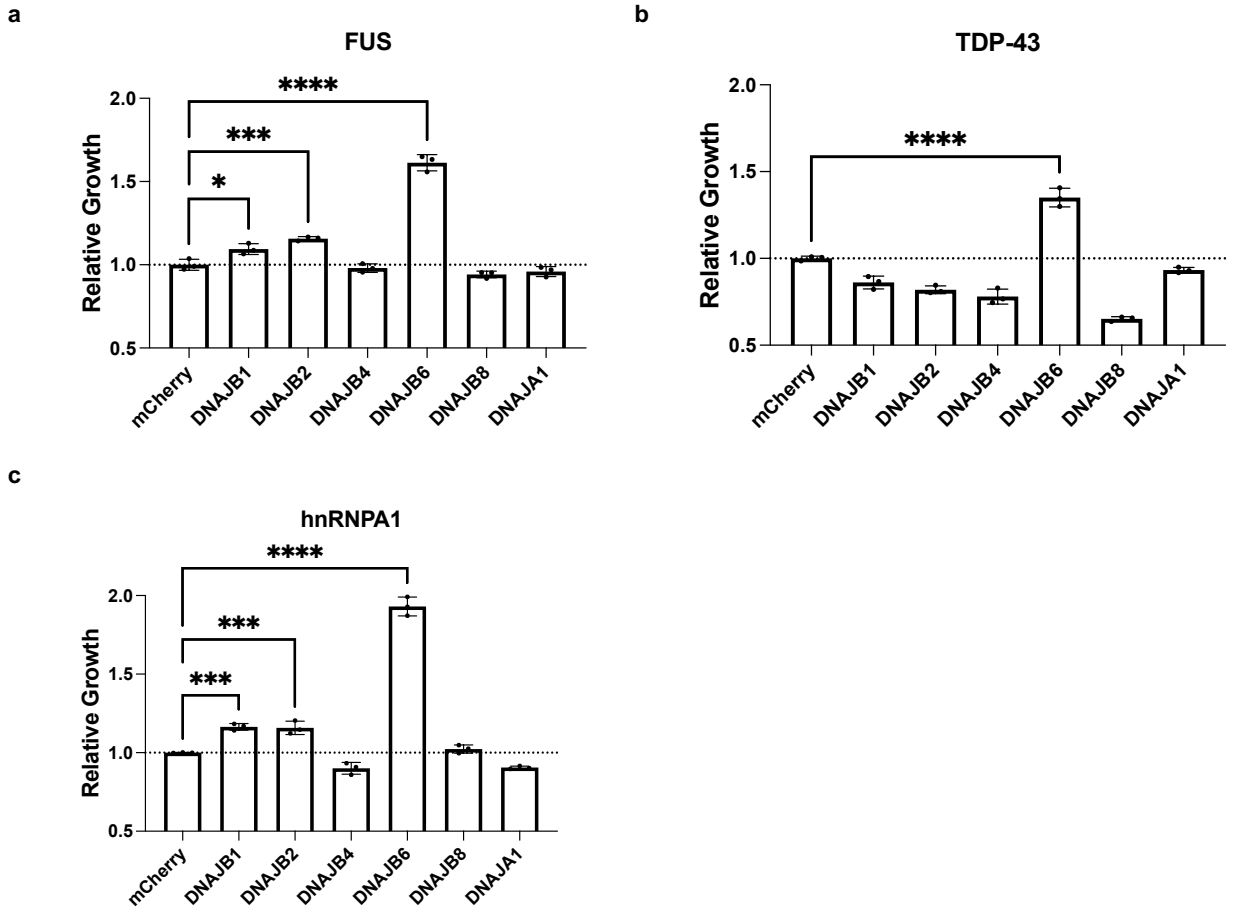

1170 **Supplementary Figure 13. RNA-seq demonstrates that DNAJB6 is significantly upregulated in**
1171 **response to FUS or TDP-43 overexpression in HEK293T cells.** Volcano plots for HEK293T expressed
1172 chaperones for **a.** FUS and **b.** TDP-43 compared to EYFP overexpressing cells. Two biological replicates
1173 were done for each condition.

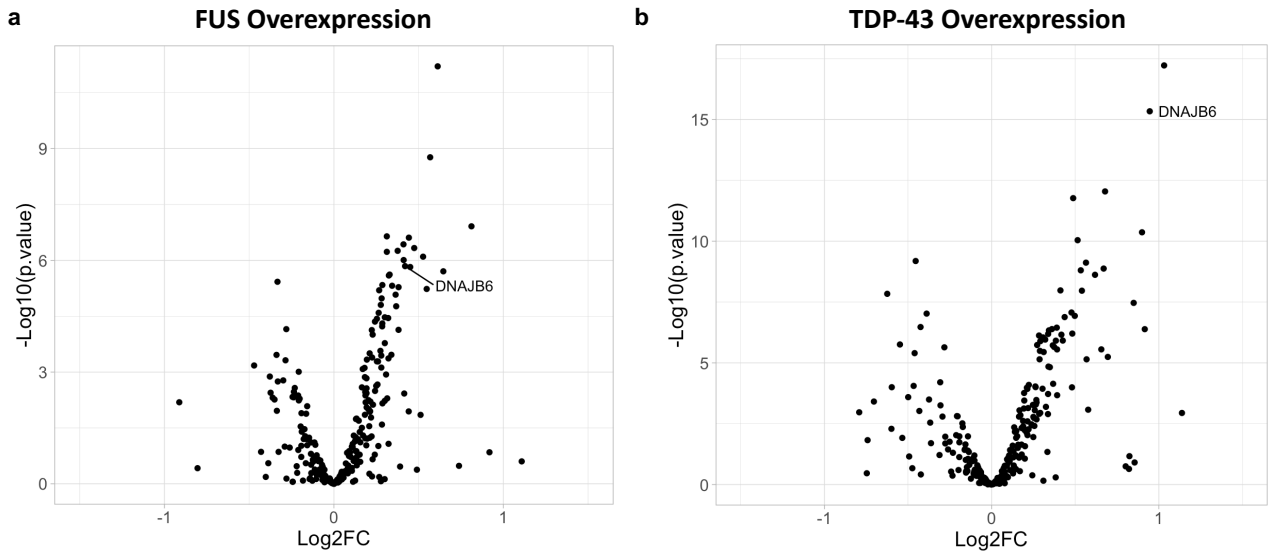

1174

1175 **Supplementary Figure 14. Knockout of DNAJB6 does not impact SDS solubility of endogenously**
1176 **expressed FUS, TDP-43, or hnRNPA1 in HEK293T cells.** HEK293T NTC and DNAJB6 KO cells were
1177 transfected with an EYFP expression vector and endogenous levels of TDP-43, FUS, and hnRNPA1 were
1178 assessed.

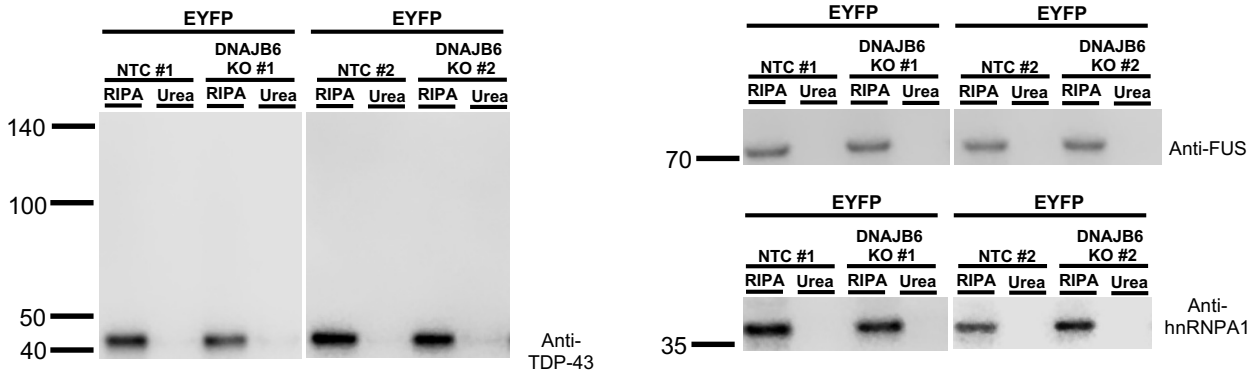

1179

1180 **Supplementary Figure 15. Biophysical characterization of DNAJB6 with clients**. **a**. DNAJB6 at 3 μM
1181 concentration undergoes LLPS at physiological salt concentrations, sample imaged 30 minutes after dilution.
1182 **b.** Ability of AF555 labeled DNAJB6 at 0.25 μM to LLPS in 500 mM NaCl and "physiologic" 50 mM NaCl
1183 conditions. Samples were imaged at 30 minutes. Scale bar represents 5 microns. **c.** FUS-mEmerald and
1184 AF555 labeled DNAJB6 co-mingle when mixed at physiological salt concentrations and at an endogenous
1185 (6:1) ratio, 1.5 μM and 0.25 μM, respectively. Scale bar represents 10 microns. Samples were imaged 20
1186 minutes after mixing. **d.** FUS-mEmerald (1.5 μM) alone and FUS-mEmerald + DNAJB6 (1.5 μM + 0.25 μM)
1187 condensates were subjected to FRAP 30 minutes after condensate formation.

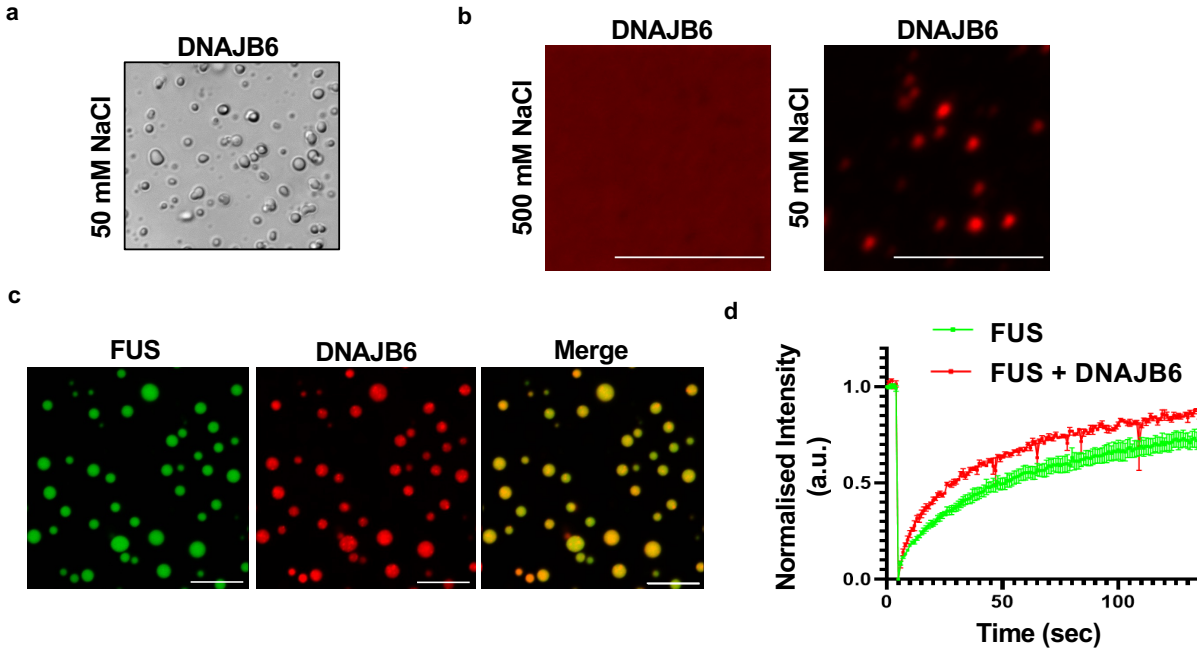

1188

Supplementary Figure 16. Example of AFM-IR nano-chemical analysis on single FUS+DNAJB6 condensates. Maps of **a.** 3-D morphology, **b.** IR absorption in the Amide I (1655cm-1), **c.** Contact resonance by phase locked loop (PLL). **d.** IR spectra from 10 independent locations (each location 5 co-averaged spectra) on the condensate, **e.** their average + SE and **f.** second derivative of the amide I band to deconvolve protein secondary structure contributions. **g.** 3-D morphology maps of 3 independent FUS and FUS + DNAJB6 condensates

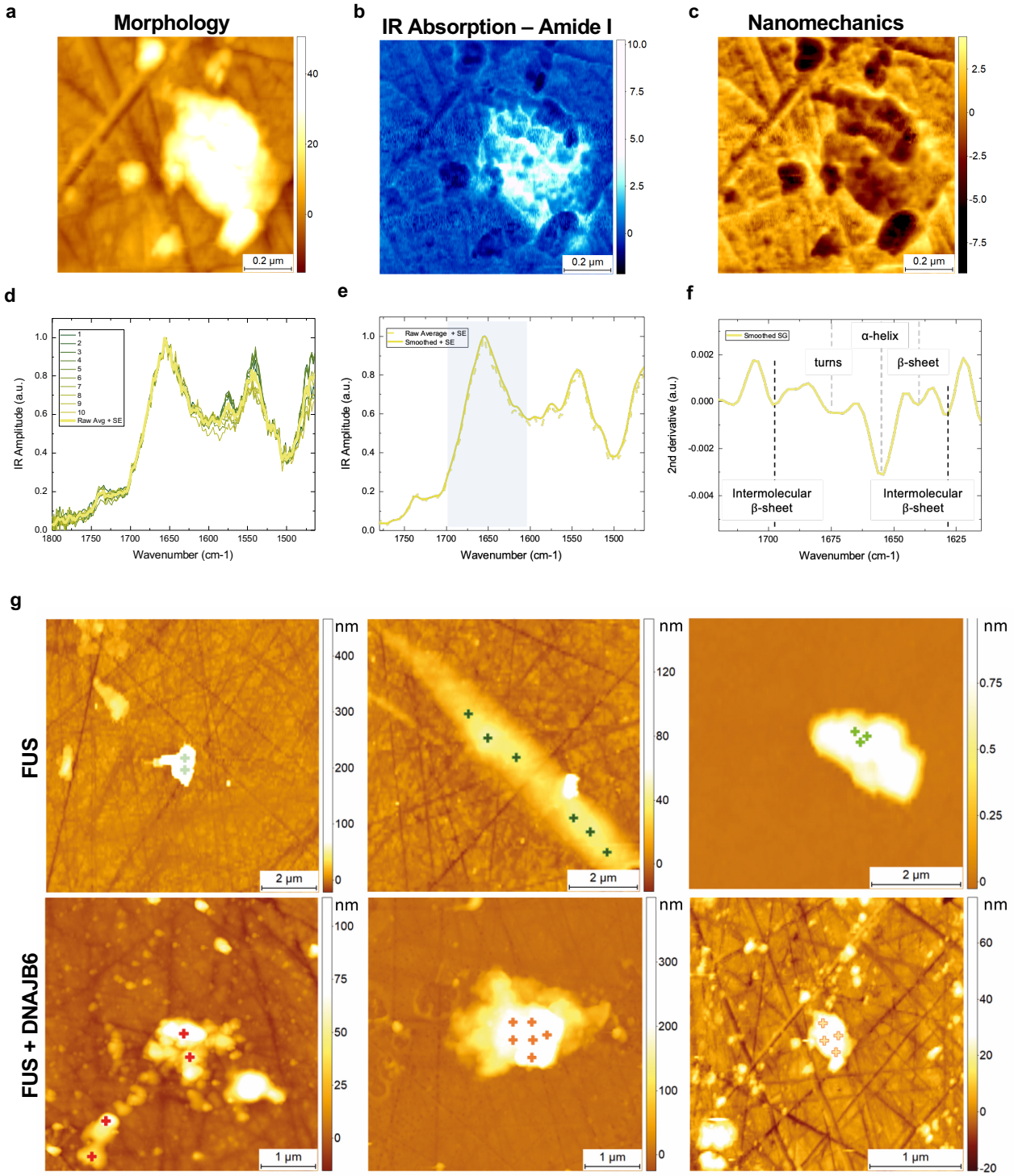

1196 **Supplementary Figure 17. Identification of DNAJB6 domains important for activity in yeast. a.** Testing
1197 domain deletions and J domain H31Q loss of function point mutant for their ability to rescue the FUS
1198 expressing yeast model. ΔJ, ΔG/F, ΔS represent deletion of the J-domain, glycine-phenylalanine rich, or
1199 serine rich region of DNAJB6, respectively. **b.** Expression confirmation of DNAJB6 and mutant variants.
1200 Comparisons were conducted with ordinary one-way ANOVA; ns = not significant, ***P≤0.001, ****P≤0.0001.

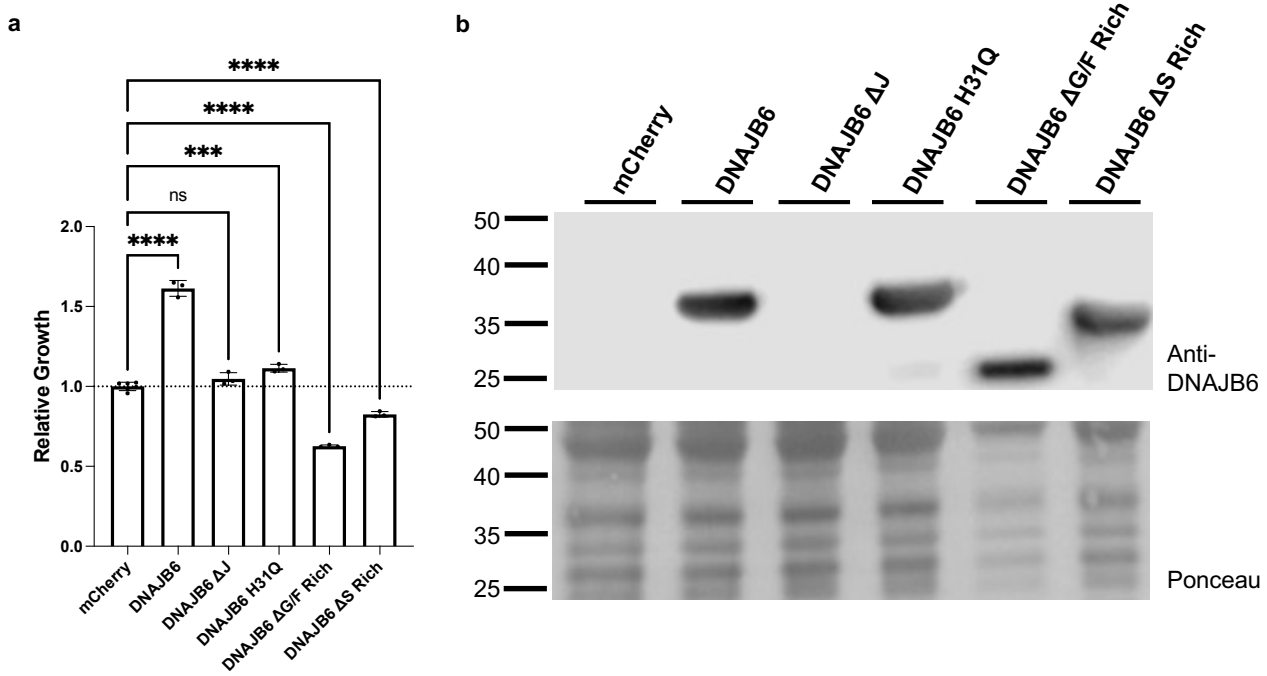

1201
1202

1203 **Supplementary Figure 18. Correlation statistics between biological replicates of deep mutational**
1204 **scan of DNAJB6. a.** Correlation between log2 fold changes for all amino acid changes at all positions
1205 tested in the deep mutational scanning approach. **b.** Correlation between log2 fold changes for amino acids
1206 in each set of 14 amino acids analyzed together in one sequencing batch.

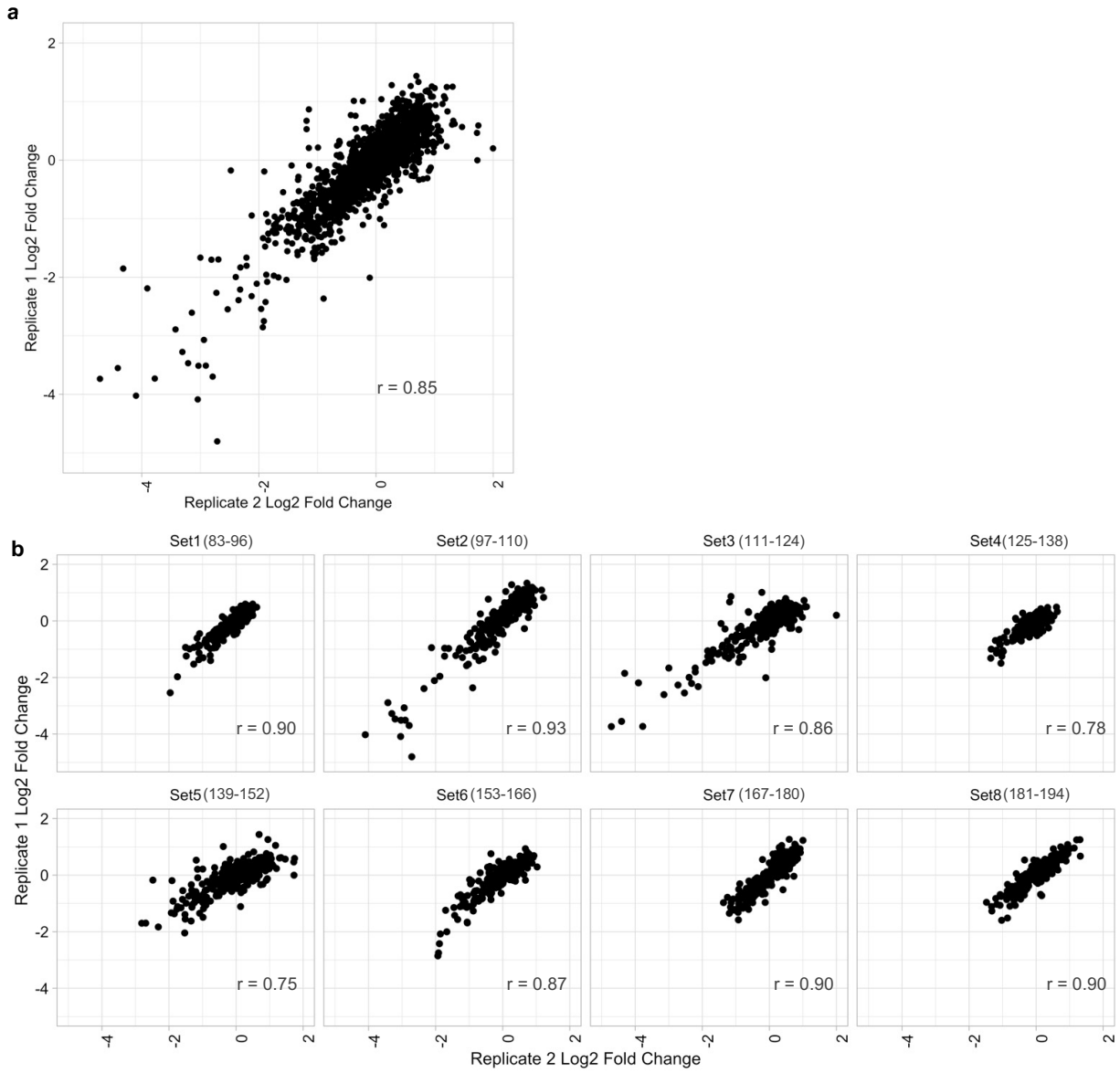

1207

1208
1209 **Supplementary Figure 19. Increasing amount of FUS plasmid transfected increases the amount of**
1210 **SDS-insoluble, Urea-soluble species.** Different doses of FUS expression plasmid were transfected and
1211 protein was harvested 48 h after transfection to assess the solubility of FUS.

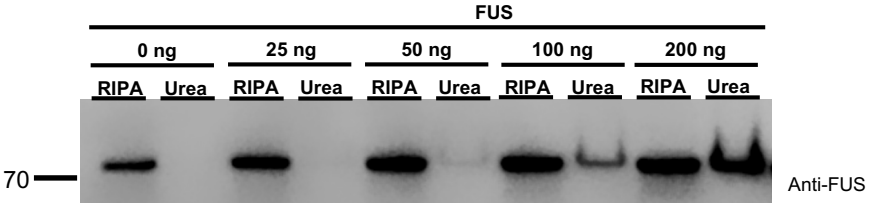

1212

Supplementary Tables

Supplementary Table 1. Models included in pool. Names, sequences, and 20 bp barcodes of models in the pool. Growth and passaging conditions for each model's secondary validation are also included.

Supplementary Table 2. Results of chaperone screen. Primary data from analysis pipeline for each interaction in the chaperone screen data set. Log2FC = Log2 fold change, FDR = False Discovery Rate.

Supplementary Table 3. Results of secondary validation of called hits and suspected interactions from the chaperone screen. Three replicates for each condition were tested.

Supplementary Table 4. Results of ORFeome screen. Primary data from analysis pipeline for each interaction in the chaperone screen data set. Log2FC = Log2 fold change, FDR = False Discovery Rate.

Supplementary Table 5. Results of secondary validation of called hits and suspected interactions from the orfeome screen. Three replicates for each condition were tested.

1228 **Supplementary Note 1**

1229 To begin to establish the feasibility of multiplex high-throughput screening, we first needed to determine the
1230 reproducibility of all the required steps within the pipeline. Towards this goal, we assembled a pilot pool
1231 composed of 117 DNA-barcoded yeast strains. Among the barcoded strains in the pool were several
1232 proteotoxic models with known genetic rescuers such as yeast prions RNQ1 and SUP35, and NDD models
1233 such as FUS, TDP-43, and alpha-synuclein. Also included in this pilot pool were other proteotoxic models
1234 selected to represent a range of different strengths of toxicity to assess how variation in the amount of growth
1235 arrest caused by a model (i.e. mild, moderate, and strong), affects the reproducibility of our system. Taking
1236 advantage of the scalability of the DNA-barcoding and to help control for variation at the biological and
1237 technical levels, each model was transformed into 3 unique isogenic DNA-barcoded strains (i.e. redundantly
1238 barcoded). This allows each barcoded variant of the same model to serve as an "internal biological replicate",
1239 and for the collective behavior of all barcodes associated with the same model to be used to determine the
1240 effects of each tested genetic modifier.

1241

1242 The first set of experiments that were performed was testing whether *en masse* mating and selection of the
1243 pilot DNA-barcoded pool was consistent when performed across multiple wells each mated to the same control
1244 rescuer strain. We observed strong correlation between separately mated pools, suggesting relative barcode
1245 abundance is preserved through mating and selection (Sup. Fig. 2a-b). We next determined whether
1246 individually mated and selected diploid pools resulted in a reproducible behavior for all members of the library
1247 when inoculated into inducing media and allowed to grow back to saturation. We observed strong correlation
1248 between separately mated, selected, and outgrown pools. These data suggest that the pool shows a
1249 consistent behavior across replicate experiments and that endpoint measurements of barcode abundance can
1250 be used to make comparisons between control rescuer and active rescuer wells (Sup. Fig. 2c-d).

1251 **Supplementary Note 2**

1252 Using the pilot pool, we tested whether altering the relative abundance of particular strains in the pool might
1253 improve our ability to detect known, literature-reported interactions between molecular chaperones and the
1254 library of proteotoxic models [27,78,79]. The "All" pooling strategy evenly mixed all 117 strains. The "Low" pooling
1255 strategy evenly mixed all strains but excluded a number of control yeast strains expressing proteins that lack
1256 toxicity (e.g. enhanced yellow fluorescent protein) to enable more division opportunities before the pool
1257 reached growth saturation. The "Skew" pooling strategy mixed all 117 strains but seeded strong and
1258 moderately toxic models at a higher initial abundance compared to the mild and non-toxic models. We
1259 observed comparable performance between the Low and All pools, with 16/17 and 14/17 literature-reported
1260 positive controls demonstrating positive log2 fold change when the behavior of all the DNA-barcodes
1261 associated with the same model were averaged (Sup. Fig. 3a). In sharp contrast, the Skew pool showed the
1262 worse performance detecting only 12/17 positive control interactions, along with showing overall lower log2
1263 fold changes as compared to the Low and All pools.

1264

1265 Upon further examination of the resulting data, a stronger correlation between biological replicates using the
1266 Low pooling strategy mated to the same benign rescuer over other strategies was observed (Sup. Fig. 3b).
1267 Additional analysis was performed in which the relationship between the coefficient of variation (CV) of a
1268 barcode and its mean relative abundance in the pool was examined. As previously shown in both RNA-
1269 sequencing and microbiome sequencing datasets, low abundance members in a mixed pool tend to show
1270 higher variance in their abundance values, which we hypothesize may render more toxic models within the
1271 pool (which are rapidly depleted during outgrowth) more variable [80,81]. The ability of a pooling strategy to
1272 reduce variability at all sampling levels, in particular those with lower abundance, suggests it should have
1273 improved performance and increased sensitivity to detect real interactions. The Low pooling strategy was
1274 generally associated with lower variability for barcodes at all relative abundances. The Skew strategy did
1275 reduce the variability of lowly abundant barcodes primarily associated with highly toxic models compared to
1276 the All pooling strategy, but was also associated with higher variability for less toxic, generally more abundant
1277 models possibly as a result of their lower initial seeding (Sup. Fig. 3c).

1278

1279 Taking the Low pooling strategy forward, we assessed sources of biological and technical noise. For this
1280 study, we considered a biological replicate to require a separate mating, selection, outgrowth, DNA harvest,
1281 and PCR amplification for sequencing. We considered technical replicates to be separate PCR amplification
1282 reactions performed on the same harvested DNA for sequencing. We observed relatively minor sources of
1283 both biological and technical variation (Sup. Fig. 4a). We also assessed whether averaging between multiple
1284 biological or technical replicates improved the reproducibility of the screen by reducing the CV ~ relative
1285 abundance relationship of barcoded strains. Averaging relative abundances of barcode strains between
1286 multiple replicates reduced the variability of barcoded strains, with averaging between 2 replicates conferring

1287 a similar advantage to averaging between 3 replicates (Sup. Fig. 4b-c). This suggested that a screening
1288 paradigm that adopts the Low pooling strategy with two biological replicates for each well and two technical
1289 replicates for each biological replicate is optimized for sensitive detection of genetic modifiers of proteotoxicity.
1290 We tested whether the Low pooling strategy along with two biological or technical replicates improved
1291 performance over the initial pilot experiment and observed that log2 fold changes were stronger and captured
1292 all known interactions (Sup. Fig. 5a). We validated, via spot assay, all potential interactions within this pilot
1293 interaction space and observed strong concordance with screen data (Sup. Fig. 5b-g)

1294 **Supplementary Note 3**

1295 The initial variance modeling data suggested that lower abundance members of the pool are highly variable
1296 and would restrict the assay to detecting only strong interactions for these models. We hypothesized that
1297 merging information between isogenic "redundantly barcoded" strains would help improve the detection of
1298 mild and moderate interactions for lower abundance pool members. Using the prior association of CV ~ relative
1299 abundance, we modeled the necessary fold change in order to detect statistically significant enrichment of
1300 models while also accounting for the large degree of multiple hypothesis testing when implementing the
1301 approach. To model the required fold change to detect significant interactions at an $\alpha = 0.05$ with a pool of 50
1302 models, we determined the multiple hypothesis corrected Z-score necessary to reach significance with a
1303 Bonferroni correction. From this Z-score, we derived the necessary fold change required to reach significance
1304 from the CV at each relative abundance. To model sharing information between barcodes, we used Stouffer's
1305 Z-score method to simulate the required individual Z-scores necessary for significance when these Z-scores
1306 are combined. Without information sharing between isogenic redundantly barcoded strains containing the
1307 same model, greater than 2-fold change in abundance was necessary for significance for lowly abundant
1308 barcodes. Our modeling suggested that information sharing between isogenic strains representing the same
1309 model would enable more sensitive detection of weaker interactions, similar to how information is shared
1310 between multiple gRNAs in CRISPR screens to identify essential genes [76]. By pooling information between 5
1311 or more isogenic strains, we determined that rescuers that increased the abundance of a model within the
1312 mixed pool by 1.5 fold could be detected with statistical significance (Sup. Fig. 6). With this approach, we
1313 observed that the benefits of redundant barcoding scaled faster than the penalties of multiple testing,
1314 suggesting that additional redundant barcoding is favorable for sensitive detection of interactions.

1315

1316 For each model, we assembled 5-7 individual barcoded strains and validated equal growth between isogenic
1317 strains containing the same model (Sup. Table 1). We pooled a total of 302 barcoded strains and assessed
1318 the CV ~ relative abundance relationship with this new pool to determine the proper read depth. We observed
1319 a similar CV ~ relative abundance relationship between this larger pool and the pilot pool used to optimize our
1320 approach. We hypothesized that increasing the read depth of each well may also reduce the CV of lowly
1321 sampled barcodes. However, we observed similar CV ~ relative abundance profiles, with 128,000 or greater
1322 reads per well demonstrating the minimum read depth required to gain most of the benefits of increased read
1323 depth in terms of CV ~ relative abundance and number of lowly sampled barcodes that are captured (Sup.
1324 Fig. 6a-b). This suggests that lowly abundant barcoded strains may retain inherent variance as a result of the
1325 degree of proteotoxicity and growth suppression they experience. At this level of sequencing depth, 24 96-
1326 well plates can be sequenced on a single Illumina NextSeq 75bp High Output run, with an approximate cost
1327 of $0.70 per screened well.